

Optical engineering and detection of magnetism in moiré semiconductors

Tsung-Sheng Huang,¹ Andrey Grankin,¹ Yu-Xin Wang (王语馨),² and Mohammad Hafezi^{1,2}

¹Joint Quantum Institute, University of Maryland, College Park, MD 20742, USA

²Joint Center for Quantum Information and Computer Science,
University of Maryland, College Park, MD 20742, USA

(Dated: April 21, 2025)

We present a general framework for optically inducing, controlling, and probing spin states in moiré systems. In particular, we demonstrate that applying Raman optical drives to moiré transition metal dichalcogenide bilayers can realize a class of spin models, with magnetic interactions tunable via the optical parameters. The resulting interaction anisotropy, controlled by the polarizations of the drives, enables access to magnetic states that are inaccessible in undriven moiré bilayers. Furthermore, we establish direct connections between the resulting spin correlations and experimentally observable optical signals. Our work paves the way for future studies on the optical control and detection on strongly correlated quantum systems.

Introduction. — Ultracold atoms in optical lattices have proven to be an exceptionally powerful platform for exploring a wide range of models, from generalized Heisenberg spin and Fermi-Hubbard models [1] to various topological systems [2]. These advances have been made possible through the optical engineering of diverse Hamiltonians, including tunneling and interaction terms [3, 4].

Motivated by these developments, an intriguing question arises: Can similar optical control be applied to a many-electron system and induce, modify and probe correlated phenomena [5]? Specifically, is it possible to optically induce and probe magnetism, by building upon a microscopic model of light-matter interaction?

Moiré transition metal dichalcogenide (TMD) bilayers [6–8], which offers a rich landscape of strong correlations [8], provide a promising platform for this investigation. The nonlinearities of electrons [9, 10] and excitons [11–14] in these systems enable the emergence of generalized Fermi-Hubbard [9, 15, 16] and generalized Bose-Hubbard [17–19] physics, respectively, and their co-existence allows for the realization of Bose-Fermi mixtures [20–22]. Importantly, spin-resolved observables from these correlated phenomena, where spins are locked to valley pseudospins via spin-orbit coupling [23], may be optically probed [24] or controlled by exploiting the selectivity in TMD heterostructures: direct transitions at valley pseudospin $\tau = +$ ($\tau = -$) primarily couple to photons with circular polarization σ_+ (σ_-) [25].

In this work, we propose how various spin models can be optically engineered in moiré TMDs, as sketched in Fig.1(a). Specifically, we focus on hole-doped heterobilayers at half-filling, where the Fermi-Hubbard gap U emerges within the first valence moiré band (VMB)[9]. Two light fields with frequencies ω and $\omega - \delta - U$ induce Raman transitions between the lower and upper Hubbard bands within VMB and the first conduction moiré band (CMB). For instance, as shown in Fig. 1(b), a σ_+ -polarized photon with frequency ω can virtually excite a $\tau = +$ electron from VMB to CMB. The charge can then return via the same photon, causing an AC Stark

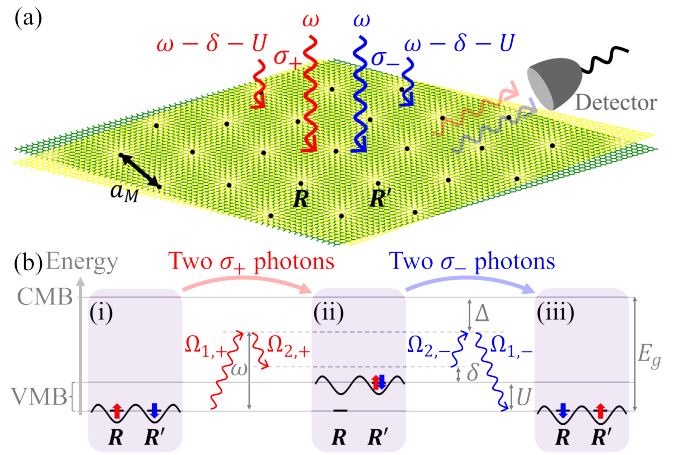


FIG. 1. Illustration of the system. (a) A moiré heterobilayer with superlattice spacing a_M driven by two external light sources at distinct frequencies ω and $\omega - \delta - U$. Emitted photons are collected by the detector. \mathbf{R} and \mathbf{R}' denote moiré sites. (b) The two-photon Raman processes inducing spin exchanges in the valence moiré band (VMB). In the presence of a charge gap U , VMB splits into upper and lower Hubbard bands. Up- and down-arrows located at the moiré sites denote VMB electrons at $\tau = +$ and $-$ valleys, respectively. A photon at frequency ω enables transition from the lower Hubbard band to a virtual state detuned from the conduction moiré band (CMB) by $\Delta = E_g - \omega$, and a photon at $\omega - \delta - U$ couples such virtual state to another that is detuned from the upper Hubbard band by δ . $\Omega_{\lambda,\tau}$ with $\lambda \in \{1, 2\}$ and $\tau \in \{\pm\}$ labels the components of the drives. Black curves indicate the moiré landscape for VMB.

shift, or create a VMB double occupancy at another site with a $\omega - \delta - U$ drive at the same polarization. Notably, this optically induced tunneling occurs only if the initial and final site spins do not form a triplet state. The double occupancy can be eliminated via the reverse process, driven by either the same- (σ_+) or opposite- (σ_-) polarized photons. While the former induces $\hat{S}_{\mathbf{R}}^z$ and $\hat{S}_{\mathbf{R}'}^z$ contributions, the latter yields $\hat{S}_{\mathbf{R}}^x \hat{S}_{\mathbf{R}'}^x + \hat{S}_{\mathbf{R}}^y \hat{S}_{\mathbf{R}'}^y$,

where $\hat{S}_{\mathbf{R}}^j$ represents the VMB spins at supersite \mathbf{R} and orientation $j \in \{x, y, z\}$.

We show that this scenario realizes a triangular lattice XXZ model [26, 27], with spin-spin interactions tunable via external drives. Their strength can be enhanced by adjusting drive intensities and frequencies, making magnetism more robust and experimentally accessible. Moreover, the interaction anisotropy is tunable via the drive polarizations, enabling previously unexplored magnetic phases in moiré TMDs. This highlights how optical control can further advance the prospect of quantum simulation in moiré TMDs. Finally, we show that these driven magnetic correlations can be probed through optical observables, specifically the intensity of Stokes sideband emission [28]. This method provides a more direct signature of magnetic phases compared to the conventional reflective magnetic circular dichroism measurement and Curie-Weiss analysis [15, 29, 30], which does not reveal interaction anisotropy.

Two-band model. — We investigate a TMD heterobilayer where electronic interaction in the highest valence moiré band (VMB) is described by an on-site Hubbard repulsion [9]. For simplicity, we focus on optical transitions between the VMB and the lowest conduction moiré band (CMB), assuming others are detuned and hence negligible. To exploit valley-polarization selectivity [25], we further consider *intralayer* VMB and CMB. Such a configuration can be realized in heterobilayers with type-I band alignment, such as MoSe₂/WS₂ [31].

With these considerations, we construct the two-band model \hat{H} :

$$\hat{H} = \hat{U} + E_g \sum_{\mathbf{L}, \tau} \hat{c}_{\mathbf{L}, \tau}^\dagger \hat{c}_{\mathbf{L}, \tau} + \hat{V}_{\text{LM}} + \hat{H}_{\text{ph}}, \quad (1)$$

where $\hat{U} = U \sum_{\mathbf{R}} \hat{n}_{\mathbf{R},+} \hat{n}_{\mathbf{R},-}$ with $\hat{n}_{\mathbf{R},\tau} = \hat{v}_{\mathbf{R},\tau}^\dagger \hat{v}_{\mathbf{R},\tau}$ denoting the number operators of electrons in VMB and U denoting their Hubbard interaction. $\tau \in \{\pm\}$ labels the valley pseudospin. $\{\mathbf{L}\}$ and $\{\mathbf{R}\}$ are the set of triangular superlattice sites of CMB and VMB electrons, respectively, which may either coincide or be shifted, depending on the material and stacking configuration [32, 33]. E_g represents the bandgap. The Hamiltonian for free electromagnetic field \hat{H}_{ph} is later eliminated by going to the interaction picture, and accordingly, the electric field operator becomes time dependent, which we express as $\hat{\mathbf{E}}(t) = \frac{1}{d} \sum_{\tau} \Omega_{\tau}(t) \mathbf{e}_{\tau} + \delta \hat{\mathbf{E}}$. Here d is the transition dipole associated to the atomic orbitals of CMB and VMB, $\Omega_{\tau}(t)$ represents the component of (spatially homogeneous) classical drive at polarization $\mathbf{e}_{\tau} = \frac{\mathbf{e}_x + i\tau \mathbf{e}_y}{\sqrt{2}}$ (with \mathbf{e}_x and \mathbf{e}_y being Cartesian unit vectors in the plane), and $\delta \hat{\mathbf{E}}$ captures the quantum fluctuations. Note that we will suppress $\delta \hat{\mathbf{E}}$ when deriving effective Hamiltonians but reintroduce it when analyzing optical detection [34]. The drives contain two frequencies ω and

$\omega - \delta - U$:

$$\Omega_{\tau}(t) = e^{-i\omega t} \left[\Omega_{1,\tau} + e^{i(\delta+U)t} \Omega_{2,\tau} \right], \quad (2)$$

with $\Omega_{\lambda,\tau}$ labeling the drive component at mode $\lambda \in \{1, 2\}$. The classical drives couple to the electrons through the following light-matter interactions (in the interaction picture) with valley-polarization selectivity [25]:

$$\hat{V}_{\text{LM}}(t) \simeq - \sum_{\tau} \sum_{\mathbf{L}, \mathbf{R}} \Omega_{\tau}(t) \eta_{\mathbf{L}, \mathbf{R}} \hat{c}_{\mathbf{L}, \tau}^\dagger \hat{v}_{\mathbf{R}, \tau} + \text{H.c.}, \quad (3)$$

where $\eta_{\mathbf{L}, \mathbf{R}}$ represents the overlap between the moiré-Wannier wavefunctions of CMB and VMB electrons centered at \mathbf{L} and \mathbf{R} , respectively [35]. Notably, the (intrinsic) tunneling of CMB and VMB electrons is ignored in Eq. (1). The former is justified, as we later focus on a detuned regime where the CMB is only virtually accessed, while the latter is weaker than a similar term induced by $\hat{V}_{\text{LM}}(t)$, as we demonstrate below.

Optically-induced tunneling. — We proceed to derive an effective model for VMB electrons from Eq. (1) in a regime where the optical drives are far off-resonant from E_g . Specifically, we consider the situation where the Raman detuning $\Delta = E_g - \omega$ and the two-photon detuning δ satisfy the following energy hierarchy:

$$|\Delta| \gg U \gg |\delta| \gg \left| \frac{\Omega_{\lambda,\tau} \Omega_{\lambda',\tau}}{\Delta} \right|. \quad (4)$$

Within these conditions, applying standard perturbation theory to Eq. (1) leads to the following effective model: [36]:

$$\hat{H}_v = \hat{U} - \xi_0 \sum_{\mathbf{R}, \tau} \Lambda_{\tau} \hat{n}_{\mathbf{R}, \tau} - \xi_1 \sum_{\tau} \sum_{\langle \mathbf{R}, \mathbf{R}' \rangle} \hat{t}_{\mathbf{R}, \mathbf{R}'}^{\tau} \hat{v}_{\mathbf{R}, \tau}^\dagger \hat{v}_{\mathbf{R}', \tau}, \quad (5)$$

where $\xi_0 = \sum_{\mathbf{L}} |\eta_{\mathbf{L}, \mathbf{R}}|^2$, and $\Lambda_{\tau} = \frac{1}{\Delta} \sum_{\lambda=1}^2 |\Omega_{\lambda,\tau}|^2$ is the AC Stark shift of the process where a VMB electron is virtually excited and then returns to its original site. $\xi_1 = \sum_{\mathbf{L}} \eta_{\mathbf{L}, \mathbf{R}}^* \eta_{\mathbf{L}, \mathbf{R}+\mathbf{a}_M}$ (with \mathbf{a}_M denoting the moiré lattice vector) represents the nearest-neighbor moiré-Wannier function overlap. Similar long-range terms are omitted in Eq. (5) as they decay exponentially with separation and are expected to be negligible relative to ξ_1 . $\hat{t}_{\mathbf{R}, \mathbf{R}'}^{\tau}$ is the optically induced nearest-neighbor density-dependent tunneling [37] with the following expression:

$$\hat{t}_{\mathbf{R}, \mathbf{R}'}^{\tau} = \begin{bmatrix} 1 - \hat{n}_{\mathbf{R}, -\tau} \\ \hat{n}_{\mathbf{R}, -\tau} \end{bmatrix}^\dagger \begin{bmatrix} \Lambda_{\tau} & \mathcal{E}_{\tau}^* \\ \mathcal{E}_{\tau} & \Lambda_{\tau} \end{bmatrix} \begin{bmatrix} 1 - \hat{n}_{\mathbf{R}', -\tau} \\ \hat{n}_{\mathbf{R}', -\tau} \end{bmatrix}, \quad (6)$$

where $\mathcal{E}_{\tau} \equiv \frac{\Omega_{2,\tau}^* \Omega_{1,\tau}}{\Delta}$ is the effective drive between the lower and upper Hubbard bands from VMB. The matrix structure in Eq. (6) captures the tunneling rates for various processes, see Fig. 2. Specifically, the diagonal terms correspond to hoppings that preserve the number

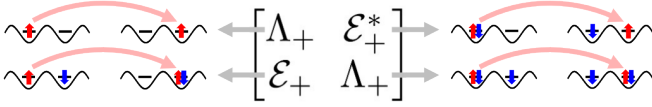


FIG. 2. Illustration of optically driven density-dependent tunneling Eq. (6) with $\tau = +$. Notation follows Fig. 1.

of double occupancies, while the off-diagonal sectors describe tunnelings that alter this number. Finally, these hopping integrals are τ -dependent and their valley contrast can be tuned by the polarization of external drives. This contrast gives rise to anisotropy in spin-spin interactions, as discussed below.

Half-filling. — When the doping concentration, controlled by the gate voltage, is tuned to one VMB electron per moiré unit cell, we can apply an additional perturbation step based on the energy hierarchy in Eq. (4) to project Eq. (5) onto the subspace where there is exactly one VMB electron per moiré unit cell [36]. This procedure yields the following effective spin model: $\hat{H}_S = -B_L \sum_{\mathbf{R}} \hat{S}_{\mathbf{R}}^z + \hat{H}_J$, where $B_L \simeq \xi_0 \sum_{\tau} \tau \Lambda_{\tau}$ is the optically induced Zeeman splitting arising from the AC Stark shift valley contrast, and \hat{H}_J captures the following spin-spin interaction of XXZ form (keeping only nearest-neighbor terms):

$$\hat{H}_J = J \sum_{\langle \mathbf{R}, \mathbf{R}' \rangle} \left[\hat{S}_{\mathbf{R}}^z \hat{S}_{\mathbf{R}'}^z + \alpha (\hat{S}_{\mathbf{R}}^x \hat{S}_{\mathbf{R}'}^x + \hat{S}_{\mathbf{R}}^y \hat{S}_{\mathbf{R}'}^y) \right], \quad (7)$$

where $\hat{S}_{\mathbf{R}}^j = \frac{1}{2} \sum_{\tau, \tau'} \hat{v}_{\mathbf{R}, \tau}^\dagger \sigma_{\tau, \tau'}^j \hat{v}_{\mathbf{R}, \tau'}$, $\forall j \in \{x, y, z\}$ are the spin operators of VMB electrons with $\sigma_{\tau, \tau'}^j$ being Pauli matrix elements. The Ising coupling J and the anisotropy in the spin-spin interaction α have the following expressions, respectively:

$$J \simeq -\frac{2|\xi_1|^2}{\delta} \sum_{\tau} |\mathcal{E}_{\tau}|^2, \quad \alpha \simeq \frac{2|\mathcal{E}_+ \mathcal{E}_-|}{|\mathcal{E}_+|^2 + |\mathcal{E}_-|^2} \cos \phi_r. \quad (8)$$

The sign of J depends on δ , and its expression suggests that XXZ magnetism becomes more robust with stronger drives or smaller detunings. In contrast, α is controlled by the polarization parameters $|\mathcal{E}_+/\mathcal{E}_-|$ and $\phi_r = \arg(\Omega_{1,-} \Omega_{2,+} \Omega_{2,-}^* \Omega_{1,+}^*)$. Note that $|\alpha| \leq 1$, with $\alpha = 1$ (Heisenberg model) and $\alpha = -1$ realized when the two drives are linearly polarized along parallel and orthogonal directions, respectively. This restriction implies that while the Ising and Heisenberg models are included in Eq. (7), the XY model is not.

The form of Eq. (7) can be justified using the symmetries of the light-matter coupling in Eq. (3). Specifically, \hat{V}_{LM} preserves the total out-of-plane magnetization, given by $\sum_{\mathbf{L}, \tau} \tau \hat{c}_{\mathbf{L}, \tau}^\dagger \hat{c}_{\mathbf{L}, \tau} + \sum_{\mathbf{R}, \tau} \tau \hat{n}_{\mathbf{R}, \tau}$ but does not generally conserve the total in-plane magnetization. After projecting out CMB states and double occupancies in VMB, the effective Hamiltonian preserves $\sum_{\mathbf{R}} \hat{S}_{\mathbf{R}}^z$ but

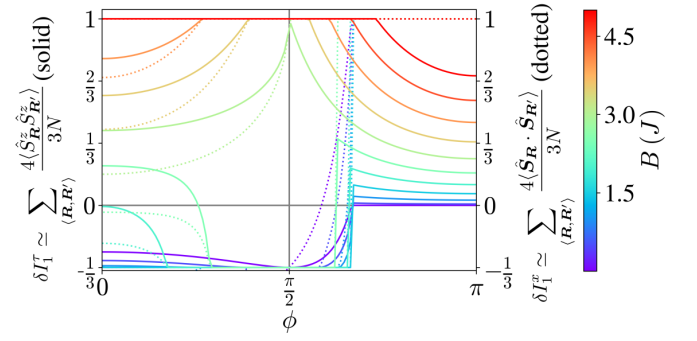


FIG. 3. Magnetic correlations from the classical mean-field ground state of Eq. (7) (see End Matter) and the corresponding relative Stokes emission intensities for $\delta < 0$. Colors label magnetic fields, with a minimum value $B = 10^{-5} J$ introduced to avoid the zero-field degeneracy.

not necessarily $\sum_{\mathbf{R}} \hat{S}_{\mathbf{R}}^x$ or $\sum_{\mathbf{R}} \hat{S}_{\mathbf{R}}^y$. Full $SU(2)$ spin rotation symmetry is preserved only when both drives are linearly polarized and perfectly aligned, resulting in an isotropic effective spin model. To further understand how each term in Eq. (7) is optically induced, we refer to the processes illustrated in Fig. 1(b). The interaction term $\sim \hat{S}_{\mathbf{R}}^z \hat{S}_{\mathbf{R}'}^z$, which splits singlet and triplet states without yielding spin exchange, arises from transitions between panels (i) and (ii) or between (ii) and (iii). Consequently, this interaction is always present unless the two drives are circularly polarized in opposite directions. In contrast, the flip-flop term $\hat{S}_{\mathbf{R}}^x \hat{S}_{\mathbf{R}'}^x + \hat{S}_{\mathbf{R}}^y \hat{S}_{\mathbf{R}'}^y$ originates from a series of processes that transforms from panel (i) to (iii). Therefore, this term requires both drives to contain components of both circular polarizations.

In the rest of this work, for the sake of concreteness we set $\Omega_{1,+} = \Omega_{1,-}$ and $\Omega_{2,+} = e^{i\phi} \Omega_{2,-}$. $\phi \in [-\pi, 0]$ is the azimuthal angle defined on the Bloch sphere of the second drive, and can be used to control $\alpha = \cos(\phi)$. Note that while the driven Zeeman splitting $B_L = 0$ in this parameter subspace, we will later introduce a real magnetic field B to mimic the role of B_L .

Optical detection. — The same setup can be utilized to measure spin correlations within the moiré system by detecting the fluctuations $\delta \hat{\mathbf{E}}(t)$. Although this approach generally applies to magnetism arising from various mechanisms (for instance, induced by intrinsic charge tunneling which we have neglected), we assume here that the drives are sufficiently strong such that Eq. (7) dominates the magnetic correlations. In this context, it is crucial to be in compliance with the energy hierarchy given by Eq. (4) to ensure the validity of the spin model.

The quantities of interest here are the intensities of the detected optical modes at frequency $\omega - U$ (also referred to as Stokes emission [28]) with polarizations filtered along \mathbf{e}_{τ} and \mathbf{e}_x , denoted as I_{τ}^T and I_{τ}^x . Using standard input-output formalism [35], one can relate this intensity to the correlators $\frac{1}{N} \sum_{\langle \mathbf{R}, \mathbf{R}' \rangle} \langle \hat{S}_{\mathbf{R}}^z \hat{S}_{\mathbf{R}'}^z \rangle$ and

$\frac{1}{N} \sum_{\langle \mathbf{R}, \mathbf{R}' \rangle} \langle \hat{\mathbf{S}}_{\mathbf{R}} \cdot \hat{\mathbf{S}}_{\mathbf{R}'} \rangle$, where N is the number of moiré sites, $\hat{\mathbf{S}}_{\mathbf{R}} = (\hat{S}_{\mathbf{R}}^x, \hat{S}_{\mathbf{R}}^y, \hat{S}_{\mathbf{R}}^z)$, and the brackets denote the expectation value with respect to the driven state. Their relative fraction of change $\delta I_1^p \equiv 1 - \frac{I_1^p}{\mathcal{I}_1^p}$ ($p \in \{x, \tau\}$), where \mathcal{I}_1^p is defined as the Stokes intensity I_1^p when the underlying spin configuration is paramagnetic, satisfy:

$$\delta I_1^\tau \simeq \sum_{\langle \mathbf{R}, \mathbf{R}' \rangle} \frac{4 \langle \hat{S}_{\mathbf{R}}^z \hat{S}_{\mathbf{R}'}^z \rangle}{3N}, \quad \delta I_1^x \simeq \sum_{\langle \mathbf{R}, \mathbf{R}' \rangle} \frac{4 \langle \hat{\mathbf{S}}_{\mathbf{R}} \cdot \hat{\mathbf{S}}_{\mathbf{R}'} \rangle}{3N}. \quad (9)$$

These relations can be qualitatively understood by noting that the effect of the detection photon on VMB electrons mimics that of $\Omega_{2,\tau}$ (except that it is incoherently emitted). Therefore, our previous arguments for the form of the effective model Eq. (7) using symmetries of light-matter coupling and Fig. 1(b) applies similarly to Eq. (9). The corresponding measurement procedure is outlined as follows: First, at the target temperature, measure the Stokes photon intensity with polarization along \mathbf{e}_τ , yielding I_1^τ . Then, raise the temperature to access a paramagnetic state and record the corresponding intensity, \mathcal{I}_1^τ . Next, repeat these measurements for Stokes photons polarized along \mathbf{e}_x , obtaining I_1^x and \mathcal{I}_1^x . The magnetic correlators are then extracted using Eq. (9). Alternatively, spin correlators can be determined without information of paramagnetic state by measuring I_1^p in extra polarization modes \mathbf{e}_p (see Supplementary Material [35]).

Signatures of the driven magnetic phases. — A fingerprint of Eq. (7) is the drastic change in its magnetic properties, and consequently in its optical responses, at the phase boundaries. To gain some physical understanding on these sharp transitions, we apply the standard three-sublattice classical mean-field treatment to the XXZ Hamiltonian, which we refer to End Matter for details. Fig. 3 shows how the relative Stokes intensities, along with spin correlators, vary with ϕ at different magnetic fields B . Significant changes and non-differentiable points appear in these optical responses, marking the phase boundaries in Fig. 3. In particular, sharp jumps in δI_1^τ and δI_1^x occur within $B \in (1.5, 3)J$, resulting from transitions between phases with opposite signs of $\frac{1}{N} \sum_{\langle \mathbf{R}, \mathbf{R}' \rangle} \langle \hat{S}_{\mathbf{R}}^z \hat{S}_{\mathbf{R}'}^z \rangle$. These abrupt changes serve as clear signatures of the driven XXZ dynamics at low temperatures, and the discussion for finite temperature is left to the End Matter.

Discussion and Outlook. — Although our analysis focuses on nearest-neighbor tunneling and spin-spin interactions, a valid treatment for large superlattice spacing, long-range optically driven contributions may become relevant in bilayers with smaller moiré periods. Notably, including next-nearest-neighbor spin-spin interactions in triangular lattices could lead to quantum spin liquids [38–40]. While similar predictions exist for undriven moiré bilayers [9], optical drives might enhance spin-spin interactions, boosting the stability of spin liquid states. Additionally, extending our two-photon probe method with

time resolution could enable detection of these states [41]. More broadly, this technique might also aid studies of other spin liquid systems beyond TMDs [42], such as those described by the Kitaev honeycomb model [43, 44].

Our scenario can be generalized to explore electronic states and dynamics away from half-filling. For instance, in lightly hole-doped regimes, valley-dependent tunneling from Eq.(6) could induce spin-valley currents, beneficial for spintronics or valleytronics applications [45]. Near half-filling, density-dependent tunneling enables independent tuning of charge excitation (doublons and holons [46]) hoppings and spin-spin interactions. This makes optically driven moiré TMDs promising for investigating phase diagrams of the paradigmatic t-J model [36, 47] and anisotropic variants like the t- J_z model [48].

An important feature of these models is the charge-spin interplay [46, 49, 50], which may be optically tuned. In particular, geometric frustration in triangular lattices makes magnetism sensitive to the sign of charge tunneling [30, 49], which in our approach is controlled by Δ . A similar effect may arise from dynamics of optical excitations (excitons) [30, 50, 51], with the key distinction that their dipolar interaction-driven tunneling [52–56] includes a valley-flip sector [57]. While suppressed in the detuned regime, this effect is expected to grow as Δ approaches the exciton binding energy. The kinetic magnetism from charge or exciton dynamics in optically driven TMDs remains an open question for future study.

Another promising direction stemming from our work is the potential application of our optical methods to manipulate other correlated states in moiré TMDs, such as Kondo insulators [58–60], fractional Chern states [61–63], and superconductivity [64, 65]. Finally, the optical approach itself can be further generalized by employing optical drives with spatial [66–68] or temporal modulation [69]. These possibilities greatly expand the scope for future exploration in strongly correlated electron-photon systems.

Acknowledgements. — We thanks Atac Imamoglu and Eugene Demler for useful discussions.

-
- [1] I. Bloch, J. Dalibard, and W. Zwerger, Many-body physics with ultracold gases, *Reviews of modern physics* **80**, 885 (2008).
 - [2] N. Cooper, J. Dalibard, and I. Spielman, Topological bands for ultracold atoms, *Reviews of modern physics* **91**, 015005 (2019).
 - [3] H. Feshbach, A unified theory of nuclear reactions. ii, *Annals of Physics* **19**, 287 (1962).
 - [4] L.-M. Duan, E. Demler, and M. D. Lukin, Controlling spin exchange interactions of ultracold atoms in optical lattices, *Physical review letters* **91**, 090402 (2003).
 - [5] J. Bloch, A. Cavalleri, V. Galitski, M. Hafezi, and A. Rubio, Strongly correlated electron–photon systems, *Nature* **606**, 41 (2022).

- [6] K. F. Mak and J. Shan, Semiconductor moiré materials, *Nature Nanotechnology* **17**, 686 (2022).
- [7] L. Du, M. R. Molas, Z. Huang, G. Zhang, F. Wang, and Z. Sun, Moiré photonics and optoelectronics, *Science* **379**, eadg0014 (2023).
- [8] D. M. Kennes, M. Claassen, L. Xian, A. Georges, A. J. Millis, J. Hone, C. R. Dean, D. Basov, A. N. Pasupathy, and A. Rubio, Moiré heterostructures as a condensed-matter quantum simulator, *Nature Physics* **17**, 155 (2021).
- [9] F. Wu, T. Lovorn, E. Tutuc, and A. H. MacDonald, Hubbard model physics in transition metal dichalcogenide moiré bands, *Physical review letters* **121**, 026402 (2018).
- [10] H. Pan, F. Wu, and S. Das Sarma, Quantum phase diagram of a moiré-hubbard model, *Physical Review B* **102**, 201104 (2020).
- [11] N. Götzing, F. Lohof, and C. Gies, Moiré-bose-hubbard model for interlayer excitons in twisted transition metal dichalcogenide heterostructures, *Physical Review B* **105**, 165419 (2022).
- [12] T.-S. Huang, P. Lunts, and M. Hafezi, Nonbosonic moiré excitons, *Physical Review Letters* **132**, 186202 (2024).
- [13] K. W. Song and O. Kyriienko, Electrically tunable and enhanced nonlinearity of moiré exciton-polaritons in transition metal dichalcogenide bilayers, *arXiv preprint arXiv:2406.08263* (2024).
- [14] K. W. Song, S. Chiavazzo, and O. Kyriienko, Microscopic theory of nonlinear phase space filling in polaritonic lattices, *Physical Review Research* **6**, 023033 (2024).
- [15] Y. Tang, L. Li, T. Li, Y. Xu, S. Liu, K. Barmak, K. Watanabe, T. Taniguchi, A. H. MacDonald, J. Shan, *et al.*, Simulation of hubbard model physics in wse₂/ws₂ moiré superlattices, *Nature* **579**, 353 (2020).
- [16] L. Wang, E.-M. Shih, A. Ghiotto, L. Xian, D. A. Rhodes, C. Tan, M. Claassen, D. M. Kennes, Y. Bai, B. Kim, *et al.*, Correlated electronic phases in twisted bilayer transition metal dichalcogenides, *Nature materials* **19**, 861 (2020).
- [17] H. Park, J. Zhu, X. Wang, Y. Wang, W. Holtzmann, T. Taniguchi, K. Watanabe, J. Yan, L. Fu, T. Cao, *et al.*, Dipole ladders with large hubbard interaction in a moiré exciton lattice, *Nature Physics* **19**, 1286 (2023).
- [18] R. Xiong, J. H. Nie, S. L. Brantly, P. Hays, R. Sailus, K. Watanabe, T. Taniguchi, S. Tongay, and C. Jin, Correlated insulator of excitons in wse₂/ws₂ moiré superlattices, *Science* **380**, 860 (2023).
- [19] B. Gao, D. G. Suárez-Forero, S. Sarkar, T.-S. Huang, D. Session, M. J. Mehrabad, R. Ni, M. Xie, P. Upadhyay, J. Vannucci, *et al.*, Excitonic mott insulator in a bose-fermi-hubbard system of moiré ws₂/wse₂ heterobilayer, *Nature Communications* **15**, 2305 (2024).
- [20] S. Miao, T. Wang, X. Huang, D. Chen, Z. Lian, C. Wang, M. Blei, T. Taniguchi, K. Watanabe, S. Tongay, *et al.*, Strong interaction between interlayer excitons and correlated electrons in wse₂/ws₂ moiré superlattice, *Nature communications* **12**, 3608 (2021).
- [21] A. B. Mhenni, W. Kadow, M. J. Metelski, A. O. Paulus, A. Dijkstra, K. Watanabe, T. Taniguchi, S. A. Tongay, M. Barbone, J. J. Finley, *et al.*, Gate-tunable bose-fermi mixture in a strongly correlated moiré bilayer electron system, *arXiv preprint arXiv:2410.07308* (2024).
- [22] P. Upadhyay, D. G. Suárez-Forero, T.-S. Huang, M. J. Mehrabad, B. Gao, S. Sarkar, D. Session, K. Watanabe, T. Taniguchi, Y. Zhou, *et al.*, Giant enhancement of exciton diffusion near an electronic mott insulator, *arXiv preprint arXiv:2409.18357* (2024).
- [23] D. Xiao, G.-B. Liu, W. Feng, X. Xu, and W. Yao, Coupled spin and valley physics in monolayers of mos₂ and other group-vi dichalcogenides, *Physical review letters* **108**, 196802 (2012).
- [24] A. G. Salvador, C. Kuhlenskamp, L. Ciorciaro, M. Knap, and A. İmamoğlu, Optical signatures of periodic magnetization: The moiré zeeman effect, *Physical Review Letters* **128**, 237401 (2022).
- [25] H. Yu, G.-B. Liu, J. Tang, X. Xu, and W. Yao, Moiré excitons: From programmable quantum emitter arrays to spin-orbit-coupled artificial lattices, *Science advances* **3**, e1701696 (2017).
- [26] D. Yamamoto, G. Marmorini, and I. Danshita, Quantum phase diagram of the triangular-lattice xxz model in a magnetic field, *Physical Review Letters* **112**, 127203 (2014).
- [27] D. Sellmann, X.-F. Zhang, and S. Eggert, Phase diagram of the antiferromagnetic xxz model on the triangular lattice, *Physical Review B* **91**, 081104 (2015).
- [28] G. Gangopadhyay and D. S. Ray, Spectral modification of the stokes line of a raman-coupled three-level system in a cavity, *Physical Review A* **45**, 1843 (1992).
- [29] E. Anderson, F.-R. Fan, J. Cai, W. Holtzmann, T. Taniguchi, K. Watanabe, D. Xiao, W. Yao, and X. Xu, Programming correlated magnetic states with gate-controlled moiré geometry, *Science* **381**, 325 (2023).
- [30] L. Ciorciaro, T. Smoleński, I. Morera, N. Kiper, S. Hiestand, M. Kroner, Y. Zhang, K. Watanabe, T. Taniguchi, E. Demler, *et al.*, Kinetic magnetism in triangular moiré materials, *Nature* **623**, 509 (2023).
- [31] J. Kang, S. Tongay, J. Zhou, J. Li, and J. Wu, Band offsets and heterostructures of two-dimensional semiconductors, *Applied Physics Letters* **102** (2013).
- [32] H. Guo, X. Zhang, and G. Lu, Shedding light on moiré excitons: A first-principles perspective, *Science advances* **6**, eabc5638 (2020).
- [33] M. H. Naik, E. C. Regan, Z. Zhang, Y.-H. Chan, Z. Li, D. Wang, Y. Yoon, C. S. Ong, W. Zhao, S. Zhao, *et al.*, Intralayer charge-transfer moiré excitons in van der waals superlattices, *Nature* **609**, 52 (2022).
- [34] Dropping the contributions of the fluctuations in the effective Hamiltonian is valid if the drives are much stronger than the spontaneous decay rate of optical excitations. In contrast, the fluctuations would yield the main contribution of the scattered photons, and need to be included for describing optical detection.
- [35] See supplementary material of this paper, which includes references [].
- [36] A. Auerbach, *Interacting electrons and quantum magnetism* (Springer Science & Business Media, 2012).
- [37] O. Dutta, M. Gajda, P. Hauke, M. Lewenstein, D.-S. Lühmann, B. A. Malomed, T. Sowiński, and J. Zakrzewski, Non-standard hubbard models in optical lattices: a review, *Reports on Progress in Physics* **78**, 066001 (2015).
- [38] W.-J. Hu, S.-S. Gong, W. Zhu, and D. Sheng, Competing spin-liquid states in the spin-1 2 heisenberg model on the triangular lattice, *Physical Review B* **92**, 140403 (2015).
- [39] S. Saadatmand, B. Powell, and I. McCulloch, Phase diagram of the spin-1 2 triangular j₁-j₂ heisenberg model on a three-leg cylinder, *Physical Review B* **91**, 245119 (2015).

- (2015).
- [40] Z. Zhu and S. R. White, Spin liquid phase of the $s=1/2$ j-1-j-2 heisenberg model on the triangular lattice, *Physical Review B* **92**, 041105 (2015).
 - [41] G. Nambiar, A. Grankin, and M. Hafezi, Diagnosing electronic phases of matter using photonic correlation functions, *arXiv preprint arXiv:2410.24215* (2024).
 - [42] L. Savary and L. Balents, Quantum spin liquids: a review, *Reports on Progress in Physics* **80**, 016502 (2016).
 - [43] A. Kitaev, Anyons in an exactly solved model and beyond, *Annals of Physics* **321**, 2 (2006).
 - [44] M. Claassen, H.-C. Jiang, B. Moritz, and T. P. Devereaux, Dynamical time-reversal symmetry breaking and photo-induced chiral spin liquids in frustrated mott insulators, *Nature communications* **8**, 1192 (2017).
 - [45] J. R. Schaibley, H. Yu, G. Clark, P. Rivera, J. S. Ross, K. L. Seyler, W. Yao, and X. Xu, Valleytronics in 2d materials, *Nature Reviews Materials* **1**, 1 (2016).
 - [46] T.-S. Huang, C. Baldwin, M. Hafezi, and V. Galitski, Spin-mediated mott excitons, *Physical Review B* **107**, 075111 (2023).
 - [47] P. A. Lee, N. Nagaosa, and X.-G. Wen, Doping a mott insulator: Physics of high-temperature superconductivity, *Reviews of modern physics* **78**, 17 (2006).
 - [48] E. Dagotto, Correlated electrons in high-temperature superconductors, *Reviews of Modern Physics* **66**, 763 (1994).
 - [49] H. Schlömer, U. Schollwöck, A. Bohrdt, and F. Grusdt, Kinetic-to-magnetic frustration crossover and linear confinement in the doped triangular t-j model, *Physical Review B* **110**, L041117 (2024).
 - [50] T.-S. Huang, Y.-Z. Chou, C. L. Baldwin, F. Wu, and M. Hafezi, Mott-moiré excitons, *Physical Review B* **107**, 195151 (2023).
 - [51] X. Wang, C. Xiao, H. Park, J. Zhu, C. Wang, T. Taniguchi, K. Watanabe, J. Yan, D. Xiao, D. R. Gamelin, *et al.*, Light-induced ferromagnetism in moiré superlattices, *Nature* **604**, 468 (2022).
 - [52] E. Shahmoon, D. S. Wild, M. D. Lukin, and S. F. Yelin, Cooperative resonances in light scattering from two-dimensional atomic arrays, *Physical review letters* **118**, 113601 (2017).
 - [53] M. Moreno-Cardoner, D. Goncalves, and D. E. Chang, Quantum nonlinear optics based on two-dimensional rydberg atom arrays, *Physical Review Letters* **127**, 263602 (2021).
 - [54] E. Sierra, S. J. Masson, and A. Asenjo-Garcia, Dicke superradiance in ordered lattices: dimensionality matters, *Physical Review Research* **4**, 023207 (2022).
 - [55] S. P. Pedersen, G. M. Bruun, and T. Pohl, Green's function approach to interacting lattice polaritons and optical nonlinearities in subwavelength arrays of quantum emitters, *Physical Review Research* **6**, 043264 (2024).
 - [56] J. Kumlin, A. Srivastava, and T. Pohl, Superradiance of strongly interacting dipolar excitons in moiré quantum materials, *Physical Review Letters* **134**, 126901 (2025).
 - [57] T.-S. Huang, Y.-X. Wang, Y.-Q. Wang, D. Chang, M. Hafezi, and A. Grankin, Collective optical properties of moiré excitons, *arXiv preprint arXiv:2407.19611* (2024).
 - [58] W. Zhao, B. Shen, Z. Tao, Z. Han, K. Kang, K. Watanabe, T. Taniguchi, K. F. Mak, and J. Shan, Gate-tunable heavy fermions in a moiré kondo lattice, *Nature* **616**, 61 (2023).
 - [59] D. Guerci, J. Wang, J. Zang, J. Cano, J. Pixley, and A. Millis, Chiral kondo lattice in doped mote2/wse2 bilayers, *Science Advances* **9**, eade7701 (2023).
 - [60] T. Devakul and L. Fu, Quantum anomalous hall effect from inverted charge transfer gap, *Physical Review X* **12**, 021031 (2022).
 - [61] J. Cai, E. Anderson, C. Wang, X. Zhang, X. Liu, W. Holtzmann, Y. Zhang, F. Fan, T. Taniguchi, K. Watanabe, *et al.*, Signatures of fractional quantum anomalous hall states in twisted mote2, *Nature* **622**, 63 (2023).
 - [62] Y. Zeng, Z. Xia, K. Kang, J. Zhu, P. Knüppel, C. Vaswani, K. Watanabe, T. Taniguchi, K. F. Mak, and J. Shan, Thermodynamic evidence of fractional chern insulator in moiré mote2, *Nature* **622**, 69 (2023).
 - [63] E. Redekop, C. Zhang, H. Park, J. Cai, E. Anderson, O. Sheekey, T. Arp, G. Babikyan, S. Salters, K. Watanabe, *et al.*, Direct magnetic imaging of fractional chern insulators in twisted mote2, *Nature* **635**, 584 (2024).
 - [64] Y. Guo, J. Pack, J. Swann, L. Holtzman, M. Cothrine, K. Watanabe, T. Taniguchi, D. Mandrus, K. Barmak, J. Hone, *et al.*, Superconductivity in twisted bilayer wse₂, *arXiv preprint arXiv:2406.03418* (2024).
 - [65] Y. Xia, Z. Han, K. Watanabe, T. Taniguchi, J. Shan, and K. F. Mak, Superconductivity in twisted bilayer wse₂, *Nature* , 1 (2024).
 - [66] F. Andreoli, C.-R. Mann, A. A. High, and D. E. Chang, Metalens formed by structured arrays of atomic emitters, *arXiv preprint arXiv:2410.22469* (2024).
 - [67] S. Sarkar, M. J. Mehrabad, D. G. Suárez-Forero, L. Gu, C. J. Flower, L. Xu, K. Watanabe, T. Taniguchi, S. Park, H. Jang, *et al.*, Sub-wavelength optical lattice in 2d materials, *arXiv preprint arXiv:2406.00464* (2024).
 - [68] D. Session, M. Jalali Mehrabad, N. Paithankar, T. Grass, C. J. Eckhardt, B. Cao, D. Gustavo Suárez Forero, K. Li, M. S. Alam, K. Watanabe, *et al.*, Optical pumping of electronic quantum hall states with vortex light, *Nature Photonics* , 1 (2024).
 - [69] C.-L. Hung, A. González-Tudela, J. I. Cirac, and H. Kimble, Quantum spin dynamics with pairwise-tunable, long-range interactions, *Proceedings of the National Academy of Sciences* **113**, E4946 (2016).
 - [70] S. Miyashita, Magnetic properties of ising-like heisenberg antiferromagnets on the triangular lattice, *Journal of the Physical Society of Japan* **55**, 3605 (1986).
 - [71] G. Murthy, D. Arovas, and A. Auerbach, Superfluids and supersolids on frustrated two-dimensional lattices, *Physical Review B* **55**, 3104 (1997).

End Matter

Appendix A: Classical mean-field theory for the XXZ model. — In this mean-field analysis, all sites $\{\mathbf{R}\}$ in the triangular lattice with periodicity a_M are categorized into three sublattice sets, with each of them being a triangular lattice with enlarged periodicity $\sqrt{3}a_M$. In addition, the operator $\hat{S}_{\mathbf{R}}$ is treated as a classical vector characterized by its polar and azimuthal angles. Therefore, the mean-field Hamiltonian contains six angular parameters. Notably, one of the three azimuthal angles can be gauged away, and therefore, effective there are only five parameters, and the mean-field ground state is determined by minimizing the energy with respect to them. Below we summarize the results for the model $\hat{H}_S = -B \sum_{\mathbf{R}} \hat{S}_{\mathbf{R}}^z + \hat{H}_J$, with \hat{H}_J given by Eq. (7).

We first summarize the solutions for $J > 0$ (and $B > 0$) following Refs. [26, 70, 71]. In this case, the ground state solutions always give coplanar spins, and therefore, without the loss of generality, we can label these solutions with the polar angles (within $\pm\pi$) of the spins in the three sublattices, which we denote as ϑ_A , ϑ_B , and ϑ_C .

For $0 < \alpha < 1$, the magnetic phases are separated by three critical magnetic fields $B_3 > B_2 > B_1 > 0$, where:

$$\begin{aligned} B_1 &= \frac{3J\alpha}{2} \\ B_2 &= \frac{3J}{2} \left[1 - \frac{\alpha}{2} + \sqrt{1 + \alpha - \frac{7}{4}\alpha^2} \right] \\ B_3 &= \frac{3J}{2}(2 + \alpha). \end{aligned} \quad (10)$$

The angular parameters from the mean-field solutions correspond to:

$$(\vartheta_A, \vartheta_B, \vartheta_C) = \begin{cases} (\pi, \vartheta, -\vartheta) & , \quad 0 < B < B_1 \\ (\pi, 0, 0) & , \quad B_1 < B < B_2 \\ (\vartheta', \vartheta'', \vartheta'') & , \quad B_2 < B < B_3 \\ (0, 0, 0) & , \quad B > B_3 \end{cases}, \quad (11)$$

where $\vartheta = \cos^{-1} \left[\frac{1 + \frac{2B}{3J}}{1 + \alpha} \right]$, and ϑ' and ϑ'' are determined by minimizing the following energy function:

$$\begin{aligned} E(\vartheta', \vartheta'') &= \frac{J}{4} [(2 \cos \vartheta' + \cos \vartheta'') \cos \vartheta'' \\ &+ \alpha (2 \sin \vartheta' + \sin \vartheta'') \sin \vartheta''] - \frac{B}{6} [\cos \vartheta' + 2 \cos \vartheta'']. \end{aligned} \quad (12)$$

Next, for $-0.5 < \alpha < 0$, there again exists three critical magnetic fields $\tilde{B}_3 > \tilde{B}_2 > \tilde{B}_1 > 0$, where:

$$\begin{aligned} \tilde{B}_1 &= \frac{3J}{4} (2 - \alpha - \sqrt{4 + 4\alpha - 7\alpha^2}) \\ \tilde{B}_2 &= J [1 - \alpha + 2\sqrt{(1 - \alpha)(1 + 2\alpha)}] \\ \tilde{B}_3 &= 3J(1 - \alpha), \end{aligned} \quad (13)$$

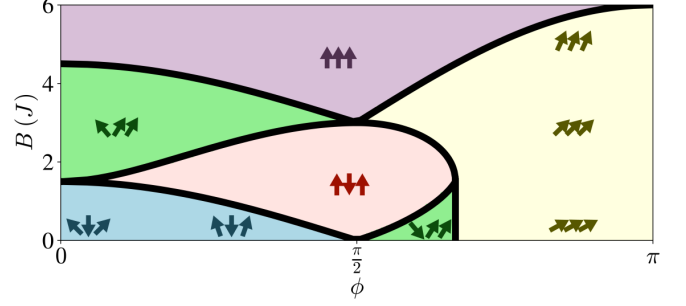


FIG. 4. Magnetic phase diagram from the classical three-sublattice mean-field ground state of Eq. (7) for $J > 0$, ranged over spin-spin interaction anisotropy $\alpha = \cos(\phi)$ and magnetic field B .

and the mean-field solutions to the ground state gives:

$$(\vartheta_A, \vartheta_B, \vartheta_C) = \begin{cases} (\vartheta', \vartheta'', \vartheta'') & , \quad 0 < B < B_1 \\ (\pi, 0, 0) & , \quad B_1 < B < B_2 \\ (\tilde{\vartheta}, \tilde{\vartheta}, \tilde{\vartheta}) & , \quad B_2 < B < B_3 \\ (0, 0, 0) & , \quad B > B_3 \end{cases}, \quad (14)$$

where $\tilde{\vartheta} = \cos^{-1}(\frac{B}{B_3})$.

Finally, for $-1 < \alpha < -0.5$, there is only one critical magnetic field B_3 , and the mean-field ground state corresponds to:

$$(\vartheta_A, \vartheta_B, \vartheta_C) = \begin{cases} (\tilde{\vartheta}, \tilde{\vartheta}, \tilde{\vartheta}) & , \quad 0 < B < B_3 \\ (0, 0, 0) & , \quad B > B_3 \end{cases}. \quad (15)$$

The magnetic phase diagram from the above expressions (for $J > 0$) is summarized in Fig. 4. It captures the essential qualitative features of the quantum phase diagram as obtained from numerical computations. Specifically, the modifications after incorporating quantum fluctuations are (1) the phase boundary at $\alpha = -0.5$ becomes B -dependent, and (2) the critical point at $(\alpha, B) = (1, 1.5J)$ split into two phase boundaries [26]. The case for $J < 0$ can be similarly analyzed, and its classical mean-field ground state simply gives a polarized spin states for all $|\alpha| \leq 1$.

Appendix B: Finite temperature. — In practice, limitations on the optical parameters might impose an upper bound on J , and the temperature T could exceed this energy scale, which is beyond the scope of the mean-field descriptions Fig. 3 and Fig. 4. To address this, we propose an alternative signature of XXZ physics that can be observed at high temperatures, where $T \gg J$. For simplicity, we focus on the case of $B = 0$. In this high-temperature regime, although the phase diagram in Fig. 4 no longer applies, the ratio between the two spin correlators in Eq. (9), and consequently $\frac{\delta I_1^x}{\delta I_1^z}$, can still

serve as an indication of spin anisotropy. Specifically, $\frac{\delta I_1^x}{\delta I_1^z}$ displays a nontrivial dependence on ϕ and approaches $1 + 2\alpha$ as T increases, as demonstrated in Fig. 5. These features provide a means of benchmarking whether the driven XXZ dynamics are accurately realized in real experimental setups.

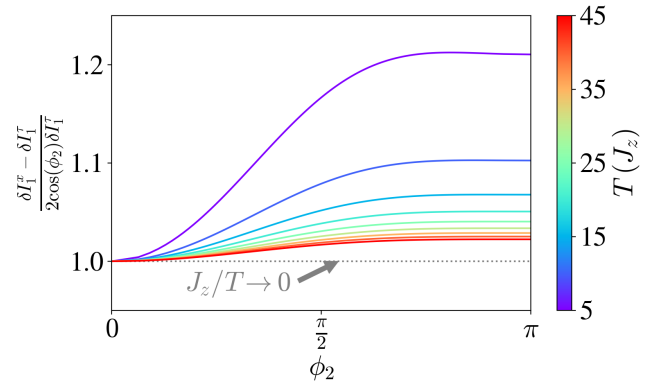


FIG. 5. Ratio between the relative Stokes signals at finite temperature T and zero magnetic field. The magnetic correlators are evaluated with a thermal state expanded in high temperature series, up to subleading order in J/T . $\Omega_{1,+} = \Omega_{1,-}$ and $\Omega_{2,+} = e^{i\phi_2} \Omega_{2,-}$ is set in this figure. Details are provided in the Supplementary Material [35].

Supplementary Material: Optical engineering and detection of magnetism in moiré semiconductors

Tsung-Sheng Huang,¹ Andrey Grankin,¹ Yu-Xin Wang (王语馨),² and Mohammad Hafezi^{1,2}

¹*Joint Quantum Institute, University of Maryland, College Park, MD 20742, USA*

²*Joint Center for Quantum Information and Computer Science,
University of Maryland, College Park, MD 20742, USA*

(Dated: April 21, 2025)

I. DERIVATION OF THE LIGHT-MATTER COUPLING

In this section, we derive the light-matter coupling in terms of superlattice degrees of freedom starting from the following microscopic description:

$$\hat{V}_{\text{LM}} = - \int d^3\mathbf{r} \hat{\mathbf{E}}(\mathbf{r}) \cdot \hat{\mathbf{P}}(\mathbf{r}), \quad \hat{\mathbf{P}}(\mathbf{r}) = -e\mathbf{r}\hat{\psi}^\dagger(\mathbf{r})\hat{\psi}(\mathbf{r}), \quad (1)$$

where $\hat{\psi}(\mathbf{r})$ is the electron field operator evaluated at (three-dimensional) position \mathbf{r} with electric charge $-e$. $\hat{\mathbf{P}}(\mathbf{r})$ and $\hat{\mathbf{E}}(\mathbf{r})$ are the polarization and electric field operators, respectively. In the following, we assume that the moiré period a_M is much larger than the monolayer lattice spacing, and the electric field varies at a length scale much greater than both of them. This allows us to address these scales separately.

To tackle the atomic scale, we decompose the electron field operator in terms of Bloch states of two (decoupled) monolayers, which are respectively labeled by their orbitals, valley pseudospins (denoted with $\tau \in \pm$), spins, and Bloch momenta. We aim at the low energy regime where spin and valley indices are locked due to spin-orbit coupling in TMDs and only the lowest conduction and the highest valence orbitals of each layer are relevant (denoted as c and v respectively). In addition, we assume that all relevant charges are *intralayer* such that the layer label can be omitted. With these considerations, we express:

$$\hat{\psi}(\mathbf{r}) \simeq \sum_{\tau} \sum_{\mathbf{p}_c} \psi_{\tau\mathbf{K}+\mathbf{p}_c}^c(\mathbf{r}) \hat{\Psi}_{\tau\mathbf{K}+\mathbf{p}_c}^c + \sum_{\mathbf{p}_v} \psi_{\tau\mathbf{K}+\mathbf{p}_v}^v(\mathbf{r}) \hat{\Psi}_{\tau\mathbf{K}+\mathbf{p}_v}^v, \quad (2)$$

where $\hat{\Psi}_{\tau\mathbf{K}+\mathbf{p}_c}^c$ and $\hat{\Psi}_{\tau\mathbf{K}+\mathbf{p}_v}^v$ are the conduction and valence electron annihilation operators respectively, with their corresponding electronic Bloch wavefunctions being $\psi_{\tau\mathbf{K}+\mathbf{p}_c}^c(\mathbf{r})$ and $\psi_{\tau\mathbf{K}+\mathbf{p}_v}^v(\mathbf{r})$. We focus on the momenta near the Brillouin zone corners $\tau\mathbf{K}$ with \mathbf{p}_n being the momentum relative to them. Note that both charges share the same set of valley momenta due to the intralayer assumption. Transforming these monolayer band degrees of freedom into the Wannier basis and then approximating atomic (in-plane) positions, denoted as \mathbf{s} , as continuous variables, we find:

$$\hat{V}_{\text{LM}} \simeq - \int d^2\mathbf{s} \hat{\mathbf{E}}(\mathbf{s}) \cdot \hat{\mathbf{P}}(\mathbf{s}), \quad \hat{\mathbf{P}}(\mathbf{s}) = \sum_{\tau} \left[\mathbf{d}_{\tau} \hat{\Psi}_{\tau}^{c\dagger}(\mathbf{s}) \hat{\Psi}_{\tau}^v(\mathbf{s}) + \text{H.c.} \right], \quad \mathbf{d}_{\tau} = -e \int d^3\mathbf{r} \psi_{\tau\mathbf{K}}^{c*}(\mathbf{r}) \mathbf{r} \psi_{\tau\mathbf{K}}^v(\mathbf{r}) = d\mathbf{e}_{\tau}^*, \quad (3)$$

where $\hat{\Psi}_{\tau}^c(\mathbf{s})$ and $\hat{\Psi}_{\tau}^v(\mathbf{s})$ are Fourier transform of $\hat{\Psi}_{\tau\mathbf{K}+\mathbf{p}_c}^c$ and $\hat{\Psi}_{\tau\mathbf{K}+\mathbf{p}_v}^v$, respectively. \mathbf{d}_{τ} is the transition dipole operator that we treated within the $\mathbf{k} \cdot \mathbf{p}$ approximation to leading order. While finding its magnitude d relies on more involved numerical calculation, its direction always aligns with $\mathbf{e}_{\tau}^* = \frac{1}{\sqrt{2}}(\mathbf{e}_x - i\tau\mathbf{e}_y)$, where \mathbf{e}_x and \mathbf{e}_y are Cartesian in-plane unit vectors, due to rotational symmetries of the wavefunctions.

We proceed by introducing moiré length scale into the above description. To do this, we expand $\hat{\Psi}_{\tau}^c(\mathbf{s})$ and $\hat{\Psi}_{\tau}^v(\mathbf{s})$ into *moiré*-Wannier orbitals (note that this is different from the monolayer Wannier orbitals). We further focus on the regime where only the first conduction and valence moiré bands (labeled as CMB and VMB respectively) are relevant [1], indicating:

$$\hat{\Psi}_{\tau}^c(\mathbf{s}) = \frac{1}{\sqrt{N}} \sum_{\mathbf{L}} W^c(\mathbf{s} - \mathbf{L}) \hat{c}_{\mathbf{L},\tau}, \quad \hat{\Psi}_{\tau}^v(\mathbf{s}) = \frac{1}{\sqrt{N}} \sum_{\mathbf{R}} W^v(\mathbf{s} - \mathbf{R}) \hat{v}_{\mathbf{R},\tau}, \quad (4)$$

where \mathbf{L} and \mathbf{R} are triangular supersites for CMB electrons and VMB holes, respectively. The two superlattices are generally different set of positions, although we assume their total number N are the same for simplicity. $W^c(\mathbf{s} - \mathbf{L})$ and $W^v(\mathbf{s} - \mathbf{R})$ are the corresponding moiré-Wannier orbitals, and $\hat{c}_{\mathbf{L},\tau}$ and $\hat{v}_{\mathbf{R},\tau}$ are the annihilation operators for these degrees of freedom, respectively. The above expression yields:

$$\hat{V}_{\text{LM}} \simeq - \sum_{\tau} \sum_{\mathbf{L},\mathbf{R}} \hat{\mathbf{E}}\left(\frac{\mathbf{L} + \mathbf{R}}{2}\right) \cdot \left[d\mathbf{e}_{\tau}^* \eta_{\mathbf{L},\mathbf{R}} \hat{c}_{\mathbf{L},\tau}^{\dagger} \hat{v}_{\mathbf{R},\tau} + \text{H.c.} \right], \quad \eta_{\mathbf{L},\mathbf{R}} = \int d^2\mathbf{s} W^{c*}(\mathbf{s} - \mathbf{L}) W^v(\mathbf{s} - \mathbf{R}). \quad (5)$$

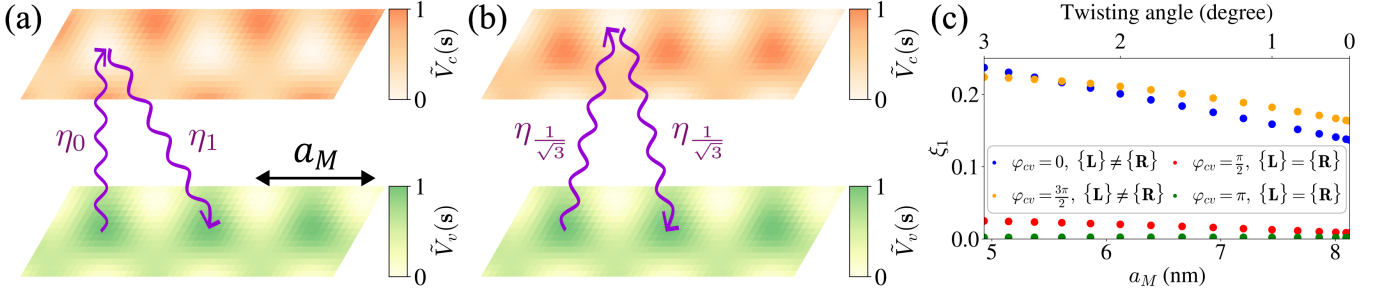


FIG. 1. Illustration of (a) identical and (b) shifted lattices. Here $\tilde{V}_c(\mathbf{s})$ and $\tilde{V}_v(\mathbf{s})$ denote the normalized moiré potentials from $V_c(\mathbf{s})$ and $V_v(\mathbf{s})$, respectively. Panel (c) shows ξ_1 at various φ_{cv} and a_M . Four representative values of φ_{cv} are chosen to illustrate two identical and two shifted lattices. Moiré period is related to twisting angle θ as $a_M(\theta) = \frac{a_{ML}}{\sqrt{\theta^2 + \delta_{ML}^2}}$, where a_{ML} is the average of lattice constants from the two TMD layers and δ is the mismatch between them. These parameters and others are set by the values for MoSe₂/WS₂: $a_{ML} = 0.325\text{nm}$ and $\delta_{ML} = 0.04$ [2]. The electron masses are $(m_c, m_v) = (0.43, -0.5)m_0$ [3] (with m_0 being the bare electron mass). The potential parameters are $V = 7\text{meV}$ and $\varphi_v = 35^\circ$ [4].

Note that the parameter $\eta_{\mathbf{L},\mathbf{R}}$ is expected to scale exponentially with $|\mathbf{L} - \mathbf{R}|$ and does not depend on $\mathbf{L} + \mathbf{R}$. Eq. (5) becomes Eq. (3) in the main text after incorporating the two external drives in the interaction picture. We utilize this expression to derive effective models and investigate measurement schemes.

A. Wannier orbital overlapping

In this section, we provide estimations for the moiré-Wannier orbital overlapping $\eta_{\mathbf{L},\mathbf{R}}$ defined in Eq. (5) as well as the quantity:

$$\xi_1 \equiv \xi_{\mathbf{R},\mathbf{R}'}|_{|\mathbf{R}-\mathbf{R}'|=a_M}, \quad \xi_{\mathbf{R},\mathbf{R}'} = \sum_{\mathbf{L}} \eta_{\mathbf{L},\mathbf{R}}^* \eta_{\mathbf{L},\mathbf{R}'}, \quad (6)$$

that eventually appears in the nearest-neighbor spin-spin interactions. We start by numerically solving the Bloch functions from the following Schrödinger equations capturing the motion of charges within a moiré potential ($\hbar = 1$ is set hereafter):

$$\left[-\frac{(\nabla_{\mathbf{s}} + i\mathbf{k})^2}{2m_c} + V_c(\mathbf{s}) - \mathcal{E}_{\mathbf{k}}^c \right] u_{\mathbf{k}}^c(\mathbf{s}) = \left[-\frac{(\nabla_{\mathbf{s}} + i\mathbf{k})^2}{2m_v} + V_v(\mathbf{s}) - \mathcal{E}_{\mathbf{k}}^v \right] u_{\mathbf{k}}^v(\mathbf{s}) = 0. \quad (7)$$

Here \mathbf{k} denotes the moiré-Bloch momentum. $m_c > 0$ and $m_v < 0$ are the effective electronic masses in CMB and VMB, respectively, and $V_c(\mathbf{s})$ and $V_v(\mathbf{s})$ are the corresponding moiré potentials. These potentials, as well as the electronic eigenfunctions $u_{\mathbf{k}}^c(\mathbf{s})$ and $u_{\mathbf{k}}^v(\mathbf{s})$, are invariant under a shift in \mathbf{s} by superlattice vectors. $\mathcal{E}_{\mathbf{k}}^c$ and $\mathcal{E}_{\mathbf{k}}^v$ represent the eigenvalues. Note that here we focus only on the lowest state for CMB and highest state for VMB for each \mathbf{k} , and therefore, the band indices are suppressed.

To proceed, we phenomenologically capture the moiré potentials for *electrons* with the following expressions: [4]

$$V_c(\mathbf{s}) = V \sum_{i=1}^3 \cos(\mathbf{G}_i \cdot \mathbf{s} + \varphi_c), \quad V_v(\mathbf{s}) = V \sum_{i=1}^3 \cos(\mathbf{G}_i \cdot \mathbf{s} + \varphi_v). \quad (8)$$

Here $\mathbf{G}_1 = \frac{4\pi}{\sqrt{3}a_M} \mathbf{e}_y$, $\mathbf{G}_2 = \frac{2\pi}{a_M} (\mathbf{e}_x - \frac{\mathbf{e}_y}{\sqrt{3}})$, and $\mathbf{G}_3 = -\frac{2\pi}{a_M} (\mathbf{e}_x + \frac{\mathbf{e}_y}{\sqrt{3}})$. V denotes captures the strength of these potentials, which we assume to be the same for the two moiré bands, whereas their profiles are characterized by the phase factors φ_c and φ_v . Notably, whether the supersites for CMB and VMB ($\{\mathbf{L}\}$ and $\{\mathbf{R}\}$ respectively) are the same or different set of triangular lattice positions, which we refer to as *identical lattices* and *shifted lattices* scenarios, depends on the choices of these phases. The situations $\varphi_{cv} \equiv \varphi_c - \varphi_v = \pi$ and 0 , yielding identical and shifted lattices respectively, are illustrated in Fig. 1(a) and (b), respectively. In real experiments, each type of lattice configuration could potentially be achieved by accessing different stacking configurations [5, 6].

After solving the Bloch functions using the above potentials, the wavefunction overlap can be obtained via:

$$\eta_{\mathbf{L},\mathbf{R}} = \frac{1}{N} \sum_{\mathbf{k}} e^{i\mathbf{k} \cdot (\mathbf{L} - \mathbf{R})} \eta_{\mathbf{k}}, \quad \eta_{\mathbf{k}} \equiv \int d^2\mathbf{s} u_{\mathbf{k}}^{c*}(\mathbf{s}) u_{\mathbf{k}}^v(\mathbf{s}). \quad (9)$$

It is worth noting that the phase of $\eta_{\mathbf{k}}$ cannot be determined solely by the Schrödinger equations [7]. Nevertheless, different gauge choices generally lead to Wannier wavefunctions with different degree of localization; therefore, to validate the tight-binding approximation where $\eta_{\mathbf{L},\mathbf{R}}$ with large $|\mathbf{L} - \mathbf{R}|$ is negligible, one has to fix the phase to ensure localized Wannier wavefunctions. Here we employ a simple approach to fix the phase of $u_{\mathbf{k}}^v(\mathbf{s})$, and similarly $u_{\mathbf{k}}^c(\mathbf{s})$, by that of $\int d^2\mathbf{s} u_{\mathbf{k}}^{v*}(\mathbf{s})f(\mathbf{s})$, with $f(\mathbf{s})$ some trial functions which we choose to be a real Gaussian.

Within this treatment, we numerically confirm that $\eta_{\mathbf{L},\mathbf{R}}$ overall decrease with larger $|\mathbf{L} - \mathbf{R}|$. Importantly, this allows us to truncate the \mathbf{L} summation in Eq. (6) such that ξ_1 can be systematically computed. By taking only the leading contribution, we find $\xi_1 = \eta_1^* \eta_0 + \eta_0^* \eta_1$ for identical lattice with η_0 and η_1 being $\eta_{\mathbf{L},\mathbf{R}}$ at $|\mathbf{L} - \mathbf{R}| = 0$ and a_M , respectively. In contrast, $\xi_1 = \left| \eta_{\frac{1}{\sqrt{3}}} \right|^2$ for shifted lattice with $\eta_{\frac{1}{\sqrt{3}}}$ being $\eta_{\mathbf{L},\mathbf{R}}$ at $|\mathbf{L} - \mathbf{R}| = \frac{a_M}{\sqrt{3}}$.

Fig. 1(c) illustrates the estimated values of ξ_1 using parameters from MoSe₂/WS₂. Specifically, we fix m_c , m_v , V , and φ_v while treating a_M and φ_c as tuning parameters. The flexibility in φ_c allows for the illustration of both identical ($\varphi_c = \frac{\pi}{2}$ and π) and shifted ($\varphi_c = 0$ and $\frac{3\pi}{2}$) lattices. Generally, shifted lattices yield larger ξ_1 than identical ones, with differences reaching orders of magnitude for certain parameter sets. Overall, ξ_1 decreases as a_M increases, which can be qualitatively understood by the narrowing of Wannier function envelopes relative to a_M . Additionally, interference between Wannier function ripples can introduce non-monotonic fluctuations in $\xi_1(a_M)$, as seen in the case of $\varphi_{cv} = \pi$. Notably, for this setting, the Wannier functions $W^c(\mathbf{s} - \mathbf{L})$ and $W^v(\mathbf{s} - \mathbf{R})$ are nearly orthogonal when $\mathbf{L} \neq \mathbf{R}$ (and fully orthogonal if $m_c = -m_v$), leading to a significantly suppressed η_1 and consequently ξ_1 .

II. MEASUREMENT OF THE RAMAN-INDUCED SPIN ORDER

Here we demonstrate how to extract the magnetic correlations of VMB electrons that is induced by the two classical light sources via optical measurements. The steps of the theoretical derivation is discussed respectively in the following sections: In Section II A we first establish the input-output formalism for light scattering from electrons experiencing Hubbard interaction. We then project the scattered electromagnetic fields into detected modes in Section II B, and construct the intensities of these modes in Section II C. Finally, for comparison, we discuss a different measurement scheme targeting at the magnetic correlations that originates from the intrinsic charge motion (rather from the drives) in Section II D.

A. Derivation of input-output relation

In this section, we derive the input-output relation following Refs. [8–10]. We start with the total electric-field operator that is expressed in terms of a superposition of sectors at different frequencies ω :

$$\hat{\mathbf{E}}(\mathbf{r}) = \int d\omega \hat{\mathbf{E}}(\mathbf{r}, \omega), \quad \hat{\mathbf{E}}(\mathbf{r}, \omega) = \hat{\mathbf{E}}^+(\mathbf{r}, \omega) + \hat{\mathbf{E}}^-(\mathbf{r}, \omega), \quad \hat{\mathbf{E}}^+(\mathbf{r}, \omega) = [\hat{\mathbf{E}}^-(\mathbf{r}, \omega)]^\dagger, \quad (10)$$

where the frequency components has the following representation:

$$\hat{\mathbf{E}}^+(\mathbf{r}, \omega) = i\mu_0\omega^2 \sqrt{\frac{\epsilon_0}{\pi}} \int d^3\mathbf{r}' \sqrt{\text{Im}\{\epsilon(\mathbf{r}', \omega)\}} \mathcal{G}^\epsilon(\omega; \mathbf{r} - \mathbf{r}') \cdot \hat{\mathbf{f}}(\mathbf{r}', \omega). \quad (11)$$

Here ϵ_0 and μ_0 are electric permittivity and magnetic permeability of free space, respectively, and at this point we keep the dielectric function $\epsilon(\mathbf{r}, \omega)$ to be general and be position and frequency dependent. $\mathcal{G}^\epsilon(\omega; \mathbf{r} - \mathbf{r}')$ is the Green's tensor (propagator of electromagnetic field) that depends on the dielectric environment, which we emphasize with the superscript ϵ . $\hat{\mathbf{f}}(\mathbf{r}, \omega)$ are vectors of bosonic operators with Cartesian components $\{\hat{f}_\alpha(\mathbf{r}, \omega) | \alpha \in (x, y, z)\}$ satisfying $[\hat{f}_\alpha(\mathbf{r}, \omega), \hat{f}_{\alpha'}(\mathbf{r}', \omega')] = \delta_{\alpha, \alpha'} \delta^{(3)}(\mathbf{r} - \mathbf{r}') \delta(\omega - \omega')$.

The $\hat{\mathbf{f}}(\mathbf{r}, \omega)$ operators can be related the matter degrees of freedom through the following Heisenberg equation of motion:

$$\partial_t \check{\mathbf{f}}(\mathbf{r}, \omega, t) = -i[\check{\mathbf{f}}(\mathbf{r}, \omega, t), \check{H}(t)], \quad \check{O}(t) = e^{i\hat{H}t} \hat{O} e^{-i\hat{H}t}, \quad \hat{H} = \hat{H}_M + \hat{H}_{ph} + \hat{V}_{LM}. \quad (12)$$

Here $\hat{H}_{ph} = \int d^3\mathbf{r} \int_0^\infty d\omega \omega \hat{\mathbf{f}}^\dagger(\mathbf{r}, \omega) \hat{\mathbf{f}}(\mathbf{r}, \omega)$ is the Hamiltonian for free electromagnetic field and \hat{H}_M is the matter sector. Solution to the above equation reads:

$$\check{\mathbf{f}}(\mathbf{r}, \omega, t) = \check{\mathbf{f}}_0(\mathbf{r}, \omega, t) + \frac{\omega^2 d^*}{c^2} \sqrt{\frac{\text{Im}\{\epsilon(\mathbf{r}, \omega)\}}{\pi\epsilon_0}} \sum_{\tau, \mathbf{L}, \mathbf{R}} \eta_{\mathbf{L}, \mathbf{R}}^* \int_0^t dt' e^{-i\omega(t-t')} \check{v}_{\mathbf{R}, \tau}^\dagger(t') \check{c}_{\mathbf{L}, \tau}(t') e_{\tau} \cdot \mathcal{G}^{\epsilon*} \left(\omega; \frac{\mathbf{L} + \mathbf{R}}{2} - \mathbf{r} \right), \quad (13)$$

where $\check{f}_0(\mathbf{r}, \omega, t)$ denotes the solution in free space.

We proceed by making assumptions regarding time scales to simplify the above integral. Specifically, we will assume that the time evolution of matter operators is dominated by the following matter Hamiltonian at short time scales:

$$\hat{H}_M = U \sum_{\mathbf{R}} \hat{n}_{\mathbf{R},+} \hat{n}_{\mathbf{R},-} + E_g \sum_{\mathbf{L},\tau} \hat{c}_{\mathbf{L},\tau}^\dagger \hat{c}_{\mathbf{L},\tau}, \quad \hat{n}_{\mathbf{R},\tau} = \hat{v}_{\mathbf{R},\tau}^\dagger \hat{v}_{\mathbf{R},\tau}, \quad (14)$$

where U is the Hubbard interaction in VMB and E_g is the bandgap. Note that here we drop the quartic interactions between CMB electrons as we assume they are dilute, and suppress the tunneling of charges for simplicity. Typically $E_g \sim 1\text{eV}$ and $U \sim 10\text{meV}$. As both E_g and $E_g - U$ are much faster than the spontaneous emission rate $\gamma = \frac{|d|^2 E_g^3}{3\pi\epsilon_0 c^3} \ll 1\text{meV}$ [11], with c denoting the speed of light, the Markov approximation is valid, giving $\check{v}_{\mathbf{R},\tau}^\dagger(t') \check{c}_{\mathbf{L},\tau}(t') \simeq e^{-i(t'-t)(E_g - U\hat{n}_{\mathbf{R},-\tau})} \check{v}_{\mathbf{R},\tau}^\dagger(t) \check{c}_{\mathbf{L},\tau}(t)$ [12]. In addition, in the spirit of coarse-grained time-averaging, we replace:

$$\int_0^t dt' e^{-i(\omega - E_g + U\hat{n}_{\mathbf{R},-\tau})(t-t')} \rightarrow \zeta(E_g - U\hat{n}_{\mathbf{R},-\tau} - \omega), \quad \zeta(x) \equiv \pi\delta(x) + i\hat{\mathcal{P}}\left(\frac{1}{x}\right), \quad (15)$$

where $\hat{\mathcal{P}}(1/x)$ stands for the principal value of $1/x$ upon integration. Substituting this to Eq. (13) and rotate back to the Schroedinger representation, we find:

$$\hat{\mathbf{f}}(\mathbf{r}, \omega) \simeq \hat{\mathbf{f}}_0(\mathbf{r}, \omega) + \frac{\omega^2 d^*}{c^2} \sqrt{\frac{\text{Im}\{\epsilon(\mathbf{r}, \omega)\}}{\pi\epsilon_0}} \sum_{\tau, \mathbf{L}, \mathbf{R}} \zeta(E_g - U\hat{n}_{\mathbf{R},-\tau} - \omega) \eta_{\mathbf{L},\mathbf{R}}^* \hat{v}_{\mathbf{R},\tau}^\dagger \hat{c}_{\mathbf{L},\tau} \mathbf{e}_\tau \cdot \mathcal{G}^* \left(\omega; \frac{\mathbf{L} + \mathbf{R}}{2} - \mathbf{r} \right). \quad (16)$$

Further putting this back to Eq. (11) and exploiting the following integral relation for components of the Green's tensor:

$$\frac{\omega^2}{c^2} \int d^3\mathbf{r}' \text{Im}\{\epsilon(\mathbf{r}', \omega)\} \mathcal{G}_{\alpha,\beta}^\epsilon(\omega; \mathbf{r} - \mathbf{r}') \mathcal{G}_{\alpha',\beta}^{\epsilon*}(\omega; \mathbf{R} - \mathbf{r}') = \text{Im} [\mathcal{G}_{\alpha,\alpha'}^\epsilon(\omega; \mathbf{r} - \mathbf{R})], \quad (17)$$

we find:

$$\hat{\mathbf{E}}^+(\mathbf{r}, \omega) = \hat{\mathbf{E}}_0^+(\mathbf{r}, \omega) + \frac{i\mu_0 d^* \omega^2}{\pi} \sum_{\tau, \mathbf{L}, \mathbf{R}} \eta_{\mathbf{L},\mathbf{R}}^* \text{Im} \left[\mathcal{G}^\epsilon \left(\omega; \mathbf{r} - \frac{\mathbf{L} + \mathbf{R}}{2} \right) \right] \cdot \mathbf{e}_\tau \zeta(E_g - U\hat{n}_{\mathbf{R},-\tau} - \omega) \hat{v}_{\mathbf{R},\tau}^\dagger \hat{c}_{\mathbf{L},\tau}, \quad (18)$$

where $\hat{\mathbf{E}}_0^+(\mathbf{r}, \omega)$ is the free field associated to $\hat{\mathbf{f}}_0(\mathbf{r}, \omega)$. The total electric field can be obtained by integrating the above expression with ω . To simplify this integral, we note that for any function $f(\omega + i\nu)$ that is analytic in the complex plane (ω, ν) , one has the (Kramers-Kronig) relation $\text{Re}[f(\omega)] = \frac{1}{\pi} \int_{-\infty}^{\infty} d\omega' \hat{\mathcal{P}} \left(\frac{\text{Im}[f(\omega')]}{\omega' - \omega} \right)$ [13], which eventually yields:

$$\hat{\mathbf{E}}^+(\mathbf{r}) = \hat{\mathbf{E}}_0^+(\mathbf{r}) + \mu_0 d^* \sum_{\tau, \mathbf{L}, \mathbf{R}} \eta_{\mathbf{L},\mathbf{R}}^* (E_g - U\hat{n}_{\mathbf{R},-\tau})^2 \mathcal{G}^\epsilon \left(E_g + U\hat{n}_{\mathbf{R},-\tau}; \mathbf{r} - \frac{\mathbf{L} + \mathbf{R}}{2} \right) \cdot \mathbf{e}_\tau \hat{v}_{\mathbf{R},\tau}^\dagger \hat{c}_{\mathbf{L},\tau}. \quad (19)$$

Note that the second term contains non-linearity that comes from Hubbard interaction. In the regime $U \ll \omega_{\text{ex}}$, this simplifies to:

$$\hat{\mathbf{E}}^+(\mathbf{r}) = \hat{\mathbf{E}}_0^+(\mathbf{r}) + \hat{\mathbf{E}}_{sc}^+(\mathbf{r}), \quad \hat{\mathbf{E}}_{sc}^+(\mathbf{r}) \simeq \mu_0 d^* E_g^2 \sum_{\tau, \mathbf{L}, \mathbf{R}} \eta_{\mathbf{L},\mathbf{R}}^* \mathcal{G}^\epsilon \left(E_g; \mathbf{r} - \frac{\mathbf{L} + \mathbf{R}}{2} \right) \cdot \mathbf{e}_\tau \hat{v}_{\mathbf{R},\tau}^\dagger \hat{c}_{\mathbf{L},\tau}, \quad (20)$$

where the expression of scattered field $\hat{\mathbf{E}}_{sc}^+(\mathbf{r})$ is reminiscent of the standard input-output relation for atomic arrays [14].

B. Detection mode theory

In real experiments, photon scattering is achieved using light beams with specific profiles (such as Gaussian), and only the same mode from the scattered fields is collected. For this reason, we project Eq. (20) into such detected mode. The beam waist is assumed to be much larger than moiré period such that spatial variation of mode profile can be neglected, and the remaining nontrivial degree of freedom is its polarization. More specifically, we consider filtering

the light to polarization \mathbf{e}_p (subscript p stands for “probed mode”) before it goes into the detector, which collects light at a plane parallel to the sample at out-of-plane coordinate $z = z_p$. The associated field operators are [14]:

$$\hat{E}_p^+ \equiv \sqrt{\frac{2c\epsilon_0}{E_g A_p}} \mathbf{e}_p^* \cdot \int_{z=z_p} d^2 \mathbf{r} \hat{\mathbf{E}}^+(\mathbf{r}) = \hat{E}_{0,p}^+ + \hat{E}_{sc,p}^+, \quad \hat{E}_{sc,p}^+ = id^* \sqrt{\frac{E_g}{2c\epsilon_0 A_p}} e^{\frac{iE_g |z_p|}{c}} \sum_{\tau, \mathbf{L}, \mathbf{R}} (\mathbf{e}_p^* \cdot \mathbf{e}_\tau) \eta_{\mathbf{L}, \mathbf{R}}^* \hat{v}_{\mathbf{R}, \tau}^\dagger \hat{c}_{\mathbf{L}, \tau}, \quad (21)$$

where A_p is the area in the z_p plane in which light is collected. Note that a normalization factor $\sqrt{\frac{2c\epsilon_0}{E_g A_p}}$ is incorporated such that $\hat{E}_p^+ \hat{E}_p^+$ (again the operators with + and - superscripts are Hermitian conjugate to each other) has the notion of photon per unit time. $\hat{E}_{0,p}^+ \equiv \sqrt{\frac{2c\epsilon_0}{E_g A_p}} \int_{z=z_p} d^2 \mathbf{r} \mathbf{e}_p^* \cdot \hat{\mathbf{E}}_0^+(\mathbf{r}) = \sqrt{\frac{2cA_p \epsilon_0}{E_g}} \mathbf{e}_p^* \cdot \hat{\mathbf{E}}_0^+$ is the according projected homogeneous free field. As frequency resolution is required (see later in Section II C), the target operator is:

$$\check{E}_{sc,p}^+(\omega) \equiv \frac{1}{T} \int_{t_0}^{t_0+T} dt e^{i\omega t} \check{E}_{sc,p}^+(t), \quad \check{O}(t) = e^{i\hat{H}t} \hat{O} e^{-i\hat{H}t}, \quad (22)$$

where t_0 is the time when the detector starts to collect data and T is the time-interval for collecting data which we eventually consider as infinite. \hat{O} is some generic operator in the Schrödinger picture. To evaluate $\check{E}_{sc,p}^+(t)$, we consider the following equation of motion:

$$\partial_t [\check{v}_{\mathbf{R}, \tau}^\dagger(t) \check{c}_{\mathbf{L}, \tau}(t)] = (-i)[E_g - U \hat{n}_{\mathbf{R}, -\tau}(t)] \check{v}_{\mathbf{R}, \tau}^\dagger(t) \check{c}_{\mathbf{L}, \tau}(t) + id \mathbf{e}_\tau^* \cdot \sum_{\mathbf{R}'} \eta_{\mathbf{L}, \mathbf{R}'} \check{\mathbf{E}}^+\left(\frac{\mathbf{L} + \mathbf{R}'}{2}, t\right) \check{v}_{\mathbf{R}, \tau}^\dagger(t) \check{v}_{\mathbf{R}', \tau}(t), \quad (23)$$

where we drop the counter-rotating contributions in the last term. Substitution of Eq. (20) yields:

$$[\partial_t + i\check{h}_{\mathbf{R}, \tau}(t)] \check{v}_{\mathbf{R}, \tau}^\dagger(t) \check{c}_{\mathbf{L}, \tau}(t) + \gamma \sum_{\mathbf{L}', \mathbf{R}', \tau'} \check{\mathcal{K}}_{\mathbf{L}', \mathbf{R}', \tau'}^{\mathbf{L}, \mathbf{R}, \tau}(t) \check{v}_{\mathbf{R}', \tau'}^\dagger(t) \check{c}_{\mathbf{L}', \tau'}(t) = id \sum_{\mathbf{R}'} \eta_{\mathbf{L}, \mathbf{R}'} \mathbf{e}_\tau^* \cdot \check{\mathbf{E}}_0^+(t) \check{v}_{\mathbf{R}, \tau}^\dagger(t) \check{v}_{\mathbf{R}', \tau}(t), \quad (24)$$

where we denote:

$$\check{h}_{\mathbf{R}, \tau} = E_g - U \hat{n}_{\mathbf{R}, -\tau} - \frac{i\gamma}{2} \sum_{\mathbf{R}' \neq \mathbf{R}} |\eta_{\mathbf{L}, \mathbf{R}'}|^2 \hat{n}_{\mathbf{R}', \tau}, \quad \gamma = \frac{|d|^2 E_g^3}{3\pi\epsilon_0 c^3}, \quad (25)$$

and the dimensionless kernel $\check{\mathcal{K}}_{\mathbf{L}', \mathbf{R}', \tau'}^{\mathbf{L}, \mathbf{R}, \tau}(t)$, originating from the off-site sector of the Green’s tensor, only depends on VMB Heisenberg operators. To proceed, we consider only bare dynamics for $\check{h}_{\mathbf{R}, \tau}(t)$, which essentially gives $\check{h}_{\mathbf{R}, \tau}$, and take the input-field as the two-frequency (ω_λ with $\lambda \in \{1, 2\}$, both comparable to E_g) classical drives $\check{\mathbf{E}}_0^+(t) \rightarrow \frac{1}{d} \sum_{\lambda=1}^2 \sum_{\tau=\pm} e^{-i\omega_\lambda t} \Omega_{\lambda, \tau} \mathbf{e}_\tau$ (with $\Omega_{\lambda, \tau}$ denoting the components of the drives). Subsequently, we time-integrate Eq. (24) within the assumption that the motion within VMB are considerably slower than interband dynamics, which scale as $e^{-iE_g t}$, to implement Born-Markov approximation. Focusing on long-time dynamics (which can be achieved by setting t_0 in Eq. (22) to be far enough from initial time) and the regime where the Raman detuning $\Delta \equiv E_g - \omega_1$ satisfies $|\Delta| \gg U \gg \gamma$ (which suppresses the kernel), we find:

$$\check{v}_{\mathbf{R}, \tau}^\dagger(t) \check{c}_{\mathbf{L}, \tau}(t) \simeq \frac{d}{\Delta} \mathbf{e}_\tau^* \cdot \check{\mathbf{E}}_0^+(t) \sum_{\mathbf{R}'} \eta_{\mathbf{L}, \mathbf{R}'} \check{v}_{\mathbf{R}, \tau}^\dagger(t) \check{v}_{\mathbf{R}', \tau}(t). \quad (26)$$

Plugging this expression back to Eq. (21) and Eq. (22), we obtain:

$$\check{E}_{sc,p}^+(\omega) = \frac{id^* e^{\frac{iE_g |z_p|}{c}}}{T\Delta} \sqrt{\frac{E_g}{2\epsilon_0 c A_p}} \sum_{\lambda=1}^2 \sum_{\tau} (\mathbf{e}_p^* \cdot \mathbf{e}_\tau) \Omega_{\lambda, \tau} \sum_{\mathbf{R}, \mathbf{R}'} \xi_{\mathbf{R}, \mathbf{R}'} \hat{v}_{\mathbf{R}, \tau}^\dagger \hat{v}_{\mathbf{R}', \tau} \delta(\omega - \omega_\lambda + U \hat{n}_{\mathbf{R}, -\tau} - U \hat{n}_{\mathbf{R}', -\tau}), \quad (27)$$

which will be utilized to compute the frequency-resolved emission intensity in the following section.

C. Intensities of Stokes scattering

The standard quantity measured in frequency-resolved optical experiments is the intensity of detected modes. For simplicity, we assume that the scattered mode can be separated from the input one (for instance, using interference

technique), and therefore, the observable of interest here is $I_{sc,p}(\omega) = \langle \check{E}_{sc,p}^-(\omega) \check{E}_{sc,p}^+(\omega) \rangle$. Importantly, the delta function in Eq. (27) indicates that $I_{sc,p}(\omega)$ is nonzero only when $\omega = \omega_\lambda$, $\omega_\lambda + U$, and $\omega_\lambda - U$, which resembles Rayleigh and Stokes scattering [13, 15], respectively. We will focus only on the latter signal as it is relevant to superexchange (discussed later). These considerations yields $I_{sc,p}(\omega) \simeq I_\lambda^p \delta(\omega - \omega_\lambda + U)$, where the intensity I_λ^p has the following form if the doublons are dilute for the reference state:

$$I_\lambda^p \sim \frac{1}{A_p} \sum_{\tau, \tau'} \Phi_{\lambda, \tau}^{p*} \Phi_{\lambda, \tau'}^p \sum_{\mathbf{R} \neq \mathbf{R}'} |\xi_{\mathbf{R}, \mathbf{R}'}|^2 \langle \hat{v}_{\mathbf{R}', \tau}^\dagger \hat{v}_{\mathbf{R}, \tau} \hat{n}_{\mathbf{R}, -\tau}^v \hat{n}_{\mathbf{R}, -\tau'}^v \hat{v}_{\mathbf{R}, \tau'}^\dagger \hat{v}_{\mathbf{R}', \tau} \rangle, \quad (28)$$

where $\Phi_{\lambda, \tau}^p \equiv (\mathbf{e}_p^* \cdot \mathbf{e}_\tau) \Omega_{\lambda, \tau}$ characterizes the projection of the drives to the detection mode. Here we suppress the proportionality factor, which does not explicitly depend on the target state, the drives λ , and the parameters labeled by the detected mode; therefore it can be calibrated by measuring I_λ^p on another known spin configuration (see below). Considering coherent state for photons and taking only nearest-neighbor terms, we find:

$$I_\lambda^p \sim \frac{1}{A_p} \sum_{\tau} \left[\frac{3N}{4} |\Phi_{\lambda, \tau}^p|^2 + \sum_{\langle \mathbf{R}, \mathbf{R}' \rangle} (\Phi_{\lambda, \tau}^{p*} \Phi_{\lambda, -\tau}^p - |\Phi_{\lambda, \tau}^p|^2) \langle \hat{S}_{\mathbf{R}'}^z \hat{S}_{\mathbf{R}}^z \rangle - \Phi_{\lambda, \tau}^{p*} \Phi_{\lambda, -\tau}^p \langle \hat{\mathbf{S}}_{\mathbf{R}'} \cdot \hat{\mathbf{S}}_{\mathbf{R}} \rangle \right], \quad (29)$$

where $\hat{S}_{\mathbf{R}}^j = \frac{1}{2} \sum_{\tau, \tau'} \hat{v}_{\mathbf{R}, \tau}^\dagger \sigma_{\tau, \tau'}^j \hat{v}_{\mathbf{R}, \tau'}$ with $j \in \{x, y, z\}$ denotes the VMB spins and $\sigma_{\tau, \tau'}^j$ represents the matrix elements of Pauli operators. The above expressions connect magnetic correlations to observables in optical experiments, and below we present two ways of extracting $\frac{1}{N} \sum_{\langle \mathbf{R}, \mathbf{R}' \rangle} \langle \hat{S}_{\mathbf{R}'}^z \hat{S}_{\mathbf{R}}^z \rangle$ and $\frac{1}{N} \sum_{\langle \mathbf{R}, \mathbf{R}' \rangle} \langle \hat{\mathbf{S}}_{\mathbf{R}'} \cdot \hat{\mathbf{S}}_{\mathbf{R}} \rangle$ without the need of the proportionality factor in Eq. (29).

The first way is to eliminate such proportionality factor by accessing the paramagnetic state, where both $\langle \hat{S}_{\mathbf{R}}^z \hat{S}_{\mathbf{R}'}^z \rangle$ and $\langle \hat{\mathbf{S}}_{\mathbf{R}} \cdot \hat{\mathbf{S}}_{\mathbf{R}'} \rangle$ are zero. Denoting the value of I_λ^p in such a state as \mathcal{I}_λ^p , we find:

$$\left(1 - \frac{\sum_{\tau} \Phi_{\lambda, \tau}^{p*} \Phi_{\lambda, -\tau}^p}{\sum_{\tau} |\Phi_{\lambda, \tau}^p|^2} \right) \sum_{\langle \mathbf{R}, \mathbf{R}' \rangle} \langle \hat{S}_{\mathbf{R}}^z \hat{S}_{\mathbf{R}'}^z \rangle + \frac{\sum_{\tau} \Phi_{\lambda, \tau}^{p*} \Phi_{\lambda, -\tau}^p}{\sum_{\tau} |\Phi_{\lambda, \tau}^p|^2} \sum_{\langle \mathbf{R}, \mathbf{R}' \rangle} \langle \hat{\mathbf{S}}_{\mathbf{R}} \cdot \hat{\mathbf{S}}_{\mathbf{R}'} \rangle \simeq \frac{3N}{4} \delta I_\lambda^p, \quad \delta I_\lambda^p = 1 - \frac{I_\lambda^p}{\mathcal{I}_\lambda^p}. \quad (30)$$

One can play with the polarizations and extract $\frac{1}{N} \sum_{\langle \mathbf{R}, \mathbf{R}' \rangle} \langle \hat{S}_{\mathbf{R}}^z \hat{S}_{\mathbf{R}'}^z \rangle$ and $\frac{1}{N} \sum_{\langle \mathbf{R}, \mathbf{R}' \rangle} \langle \hat{\mathbf{S}}_{\mathbf{R}} \cdot \hat{\mathbf{S}}_{\mathbf{R}'} \rangle$ respectively from the above formula:

$$\sum_{\langle \mathbf{R}, \mathbf{R}' \rangle} \langle \hat{S}_{\mathbf{R}}^z \hat{S}_{\mathbf{R}'}^z \rangle \simeq \frac{3N}{4} \delta I_\lambda^z, \quad \sum_{\langle \mathbf{R}, \mathbf{R}' \rangle} \langle \hat{\mathbf{S}}_{\mathbf{R}} \cdot \hat{\mathbf{S}}_{\mathbf{R}'} \rangle \simeq \frac{3N}{4} \frac{\sum_{\tau} |\Omega_{\lambda, \tau}|^2}{\sum_{\tau} \Omega_{\lambda, \tau}^* \Omega_{\lambda, -\tau}} \delta I_\lambda^x + \left(1 - \frac{\sum_{\tau} |\Omega_{\lambda, \tau}|^2}{\sum_{\tau} \Omega_{\lambda, \tau}^* \Omega_{\lambda, -\tau}} \right) \sum_{\langle \mathbf{R}, \mathbf{R}' \rangle} \langle \hat{S}_{\mathbf{R}}^z \hat{S}_{\mathbf{R}'}^z \rangle, \quad (31)$$

where δI_λ^z and δI_λ^x indicates δI_λ^p with $\mathbf{e}_p = \mathbf{e}_\tau$ and $\mathbf{e}_p = \mathbf{e}_x$, respectively. By setting $\Omega_{1,+} = \Omega_{1,-}$, we arrive at the expressions for δI_1^z and δI_1^x in the main text.

Another way is to access three different probe polarizations \mathbf{e}_p . Plugging the three values of I_λ^p into Eq. (29) yields three coupled equations with three variables: the proportionality constant, $\frac{1}{N} \sum_{\langle \mathbf{R}, \mathbf{R}' \rangle} \langle \hat{S}_{\mathbf{R}}^z \hat{S}_{\mathbf{R}'}^z \rangle$, and $\frac{1}{N} \sum_{\langle \mathbf{R}, \mathbf{R}' \rangle} \langle \hat{\mathbf{S}}_{\mathbf{R}} \cdot \hat{\mathbf{S}}_{\mathbf{R}'} \rangle$. In principle, the spin correlators can also be obtained by solving these equations.

D. Measurement of the intrinsic magnetic order

In the previous sections, we discussed how to measure spin correlation *induced* by the drives, which are set off-resonantly ($\omega_1 - \omega_2 \neq U$) in order to be compatible with the realization of the XXZ model presented in the main text. On the other hand, one can instead target at the *intrinsic* magnetic correlation, induced by charge kinetic energy \hat{T} which we neglect throughout the work but (strictly speaking) is present. For such a purpose, the frequencies of optical sources can be set resonantly, i.e., $\omega_1 - \omega_2 = U$. More specifically, one can drive one of the two modes and consider absorption of the other (weak) mode. The absorption rate of such process is from a state in the lower Hubbard band (indicated by the bracket below) to the upper Hubbard band (indicated by the projector \hat{P}_U) can therefore be estimated by Fermi-golden rule as $\Gamma_{LU} \delta(U - \omega_1 + \omega_2)$, where $\Gamma_{LU} = 2\pi \langle \hat{H}_v \hat{P}_U \hat{H}_v \rangle$. Note that the terms in the bracket are quartic in VMB electrons, which turns into spin-spin interactions similar to I_λ^p discussed in the previous section. We follow the same strategy by comparing Γ_{LU} with its value in the paramagnetic state, Υ_{LU} to obtain:

$$\frac{\Gamma_{LU}}{\Upsilon_{LU}} = 1 - \frac{4}{3N} \left(1 - \frac{\sum_{\tau} \Omega_{2,-\tau}^* \Omega_{1,-\tau} \Omega_{1,\tau}^* \Omega_{2,\tau}}{\sum_{\tau} |\Omega_{1,\tau} \Omega_{2,\tau}|^2} \right) \sum_{\langle \mathbf{R}, \mathbf{R}' \rangle} \langle \hat{S}_{\mathbf{R}}^z \hat{S}_{\mathbf{R}'}^z \rangle - \frac{4}{3N} \frac{\sum_{\tau} \Omega_{2,-\tau}^* \Omega_{1,-\tau} \Omega_{1,\tau}^* \Omega_{2,\tau}}{\sum_{\tau} |\Omega_{1,\tau} \Omega_{2,\tau}|^2} \sum_{\langle \mathbf{R}, \mathbf{R}' \rangle} \langle \hat{\mathbf{S}}_{\mathbf{R}} \cdot \hat{\mathbf{S}}_{\mathbf{R}'} \rangle. \quad (32)$$

Again, by varying the polarization of the drives, one can extract different sectors of spin correlations from the measurement of $\frac{\Gamma_{\text{LU}}}{\Upsilon_{\text{LU}}}$.

III. HIGH TEMPERATURE EXPANSION FOR THE STOKES INTENSITIES

In this section, we present the calculation for high temperature expansion on the triangular lattice XXZ model at zero magnetic field:

$$\hat{H}_J = \hat{H}_z + \hat{H}_{xy}, \quad \hat{H}_z = \sum_{\langle \mathbf{R}, \mathbf{R}' \rangle} J_z \hat{S}_{\mathbf{R}}^z \hat{S}_{\mathbf{R}'}^z, \quad \hat{H}_{xy} = J_{xy} \sum_{\langle \mathbf{R}, \mathbf{R}' \rangle} (\hat{S}_{\mathbf{R}}^x \hat{S}_{\mathbf{R}'}^x + \hat{S}_{\mathbf{R}}^y \hat{S}_{\mathbf{R}'}^y), \quad (33)$$

with J_z and $J_{xy} = J_z \alpha$ denoting the spin-spin interactions. We first consider expanding the partition function $Z \equiv \text{Tr} [e^{-\beta \hat{H}_J}]$ in series of inverse temperature βJ_z up to third order $Z \simeq \sum_{n=0}^3 Z_n$. Each component reads:

$$Z_0 = 2^N, \quad Z_1 = 0, \quad Z_2 = \frac{\beta^2}{2} \text{Tr} [\hat{H}_z^2 + \hat{H}_{xy}^2], \quad Z_3 = -\frac{\beta^3}{6} \text{Tr} [\hat{H}_z^3 + 3\hat{H}_z \hat{H}_{xy}^2 + \hat{H}_{xy}^3]. \quad (34)$$

To proceed, evaluation of the traces is required.

We start by computing the terms in Z_2 , which only involves spins in two nearest-neighbor sites, and therefore, produces a 2^{N-2} factor for all terms by tracing out other sites. First, at each site, the spins have to appear as even power as $\text{Tr}[(\hat{S}_{\mathbf{R}})^n] = 0$ with odd n . Together with $\text{Tr}[(\hat{S}_{\mathbf{R}}^z)^2] = \frac{1}{2}$, we find $\text{Tr}[\hat{H}_z^2] = 2^N \times \frac{3NJ_z^2}{16}$, where we have utilized the fact that triangular lattices have $3N$ bonds in total. Similarly, with $\text{Tr}[(\hat{S}_{\mathbf{R}}^x)^2] = \text{Tr}[(\hat{S}_{\mathbf{R}}^y)^2] = \frac{1}{2}$ and $\text{Tr}[\hat{S}_{\mathbf{R}}^x \hat{S}_{\mathbf{R}}^y] = 0$, we obtain $\text{Tr}[\hat{H}_{xy}^2] = 2^N \times \frac{3NJ_{xy}^2}{8}$. In contrast, terms in Z_3 can be classified into two classes. The ones involving spins at three sites within the same triangular plaquette can be evaluated as $\text{Tr}[\hat{H}_z^3] = 2^N \times \frac{3NJ_z^3}{16}$ and $\text{Tr}[\hat{H}_{xy}^3] = 2^N \times \frac{3NJ_{xy}^3}{8}$ following the arguments above. As for the other terms involving spins in two nearest-neighbor sites, we need $\text{Tr}[\hat{S}_{\mathbf{R}}^x \hat{S}_{\mathbf{R}'}^y \hat{S}_{\mathbf{R}'}^z] = \frac{i}{4}$, which yields $\text{Tr}[\hat{H}_z \hat{H}_{xy}^2] = -2^N \times \frac{3NJ_z J_{xy}^2}{32}$. Combining all these ingredients yields:

$$\frac{Z}{2^N} = 1 + N \left[\frac{3\beta^2}{32} (J_z^2 + 2J_{xy}^2) - \frac{\beta^3}{64} (2J_z^3 + 4J_{xy}^3 - 3J_z J_{xy}^2) \right] + \mathcal{O}(\beta^4 J_z^4). \quad (35)$$

The free energy per site is then:

$$f = -\frac{1}{N\beta} \ln Z \simeq -\frac{\ln 2}{\beta} - \frac{3\beta}{32} (J_z^2 + 2J_{xy}^2) + \frac{\beta^2}{64} (2J_z^3 + 4J_{xy}^3 - 3J_z J_{xy}^2) + \mathcal{O}(\beta^3 J_z^4). \quad (36)$$

For the isotropic case where $J_{xy} = J_z = J$, we find $-\beta f \simeq \ln 2 + \frac{9(\beta J)^2}{8} + \frac{3(\beta J)^3}{8}$, consistent with reported results [16]. From the above expression, we can evaluate the following spin correlators at finite temperature:

$$\frac{1}{N} \sum_{\langle \mathbf{R}, \mathbf{R}' \rangle} \langle \hat{S}_{\mathbf{R}}^z \hat{S}_{\mathbf{R}'}^z \rangle_{\beta} = \frac{\partial f}{\partial J_z} = -\frac{3\beta}{16} J_z + \frac{3\beta^2}{64} (2J_z^2 - J_{xy}^2), \quad (37)$$

$$\frac{1}{N} \sum_{\langle \mathbf{R}, \mathbf{R}' \rangle} \left[\langle \hat{\mathbf{S}}_{\mathbf{R}} \cdot \hat{\mathbf{S}}_{\mathbf{R}'} \rangle_{\beta} - \langle \hat{S}_{\mathbf{R}}^z \hat{S}_{\mathbf{R}'}^z \rangle_{\beta} \right] = \frac{\partial f}{\partial J_{xy}} = -\frac{3\beta}{8} J_{xy} + \frac{3\beta^2}{32} (2J_{xy}^2 - J_z J_{xy}), \quad (38)$$

where $\langle \hat{O} \rangle_{\beta} \equiv \frac{1}{Z} \text{Tr} [\hat{O} e^{-\beta \hat{H}_J}]$ denotes the expectation value of the operator \hat{O} with respect to a thermal state. The ratio between these correlators can be related to the Stokes intensity via Eq. (31), giving:

$$\frac{\delta I_1^x - \delta I_1^{\tau}}{\delta I_1^{\tau}} = \alpha \frac{2 - \frac{\beta J_z}{2} (2\alpha - 1)}{1 - \frac{\beta J_z}{4} (2 - \alpha^2)}. \quad (39)$$

Within the conditions $\Omega_{1,+} = \Omega_{1,-}$ and $\Omega_{2,+} = e^{i\phi_2} \Omega_{2,-}$, the above formula yields the curves in Fig. 4 in the (End Matter of the) main text.

[1] This assumption is valid when Coulomb attraction between electrons and holes are weaker than moiré potential.

- [2] Jun Kang, Sefaattin Tongay, Jian Zhou, Jingbo Li, and Junqiao Wu, “Band offsets and heterostructures of two-dimensional semiconductors,” *Applied Physics Letters* **102** (2013).
- [3] Sara Conti, David Neilson, François M Peeters, and Andrea Perali, “Transition metal dichalcogenides as strategy for high temperature electron-hole superfluidity,” *Condensed Matter* **5**, 22 (2020).
- [4] Yang Zhang, Noah FQ Yuan, and Liang Fu, “Moiré quantum chemistry: charge transfer in transition metal dichalcogenide superlattices,” *Physical Review B* **102**, 201115 (2020).
- [5] Pranshu Upadhyay, Daniel G Suárez-Forero, Tsung-Sheng Huang, Mahmoud Jalali Mehrabad, Beini Gao, Supratik Sarkar, Deric Session, Kenji Watanabe, Takashi Taniguchi, You Zhou, *et al.*, “Giant enhancement of exciton diffusion near an electronic mott insulator,” *arXiv preprint arXiv:2409.18357* (2024).
- [6] Xi Wang, Xiaowei Zhang, Jiayi Zhu, Heonjoon Park, Yingqi Wang, Chong Wang, William G Holtzmann, Takashi Taniguchi, Kenji Watanabe, Jiaqiang Yan, *et al.*, “Intercell moiré exciton complexes in electron lattices,” *Nature Materials* **22**, 599–604 (2023).
- [7] Nicola Marzari, Arash A Mostofi, Jonathan R Yates, Ivo Souza, and David Vanderbilt, “Maximally localized wannier functions: Theory and applications,” *Reviews of Modern Physics* **84**, 1419–1475 (2012).
- [8] T Gruner and D-G Welsch, “Green-function approach to the radiation-field quantization for homogeneous and inhomogeneous kramers-kronig dielectrics,” *Physical Review A* **53**, 1818 (1996).
- [9] Ho Trung Dung, Ludwig Knöll, and Dirk-Gunnar Welsch, “Resonant dipole-dipole interaction in the presence of dispersing and absorbing surroundings,” *Physical Review A* **66**, 063810 (2002).
- [10] Ana Asenjo-Garcia, JD Hood, DE Chang, and HJ Kimble, “Atom-light interactions in quasi-one-dimensional nanostructures: A green’s-function perspective,” *Physical Review A* **95**, 033818 (2017).
- [11] Tsung-Sheng Huang, Yu-Xin Wang, Yan-Qi Wang, Darrick Chang, Mohammad Hafezi, and Andrey Grankin, “Collective optical properties of moiré excitons,” *arXiv preprint arXiv:2407.19611* (2024).
- [12] External drives are detuned following Eq. (4) of the main text such that they effectively only provide corrections to the energy of electron-hole pairs that are much smaller than E_g .
- [13] D. A. Steck, *Quantum and Atom Optics* (2007).
- [14] MT Manzoni, M Moreno-Cardoner, A Asenjo-Garcia, James V Porto, Alexey V Gorshkov, and DE Chang, “Optimization of photon storage fidelity in ordered atomic arrays,” *New journal of physics* **20**, 083048 (2018).
- [15] Gautam Gangopadhyay and Deb Shankar Ray, “Spectral modification of the stokes line of a raman-coupled three-level system in a cavity,” *Physical Review A* **45**, 1843 (1992).
- [16] Jaan Oitmaa and E Bornilla, “High-temperature-series study of the spin-1/2 heisenberg ferromagnet,” *Physical Review B* **53**, 14228 (1996).